Polarimetric Radar Observations of Simultaneous Tornadoes on 10 May 2010 near Norman, Oklahoma

CASEY B. GRIFFIN

School of Meteorology, and Advanced Radar Research Center, University of Oklahoma, Norman, Oklahoma

DAVID J. BODINE AND ROBERT PALMER

Advanced Radar Research Center, University of Oklahoma, Norman, Oklahoma

(Manuscript received 16 May 2019, in final form 21 October 2019)

ABSTRACT

This study utilizes data collected by the University of Oklahoma Advanced Radar Research Center's Polarimetric Radar for Innovations in Meteorology and Engineering (OU-PRIME) C-band radar as well as the federal KTLX and KOUN WSR-88D S-band radars to study a supercell that simultaneously produced a long-track EF-4 tornado and an EF-2 landspout tornado (EF indicates the enhanced Fujita scale) near Norman, Oklahoma, on 10 May 2010. Contrasting polarimetric characteristics of two tornadoes over similar land cover but with different intensities are documented. Also, the storm-scale sedimentation of debris within the supercell is investigated, which includes observations of rotation and elongation of a tornadic debris signature with height. A dual-wavelength comparison of debris at S and C bands is performed. These analyses indicate that lofted debris within the tornado was larger than debris located outside the damage path of the tornado and that debris size outside the tornado increased with height, likely as the result of centrifuging. Profiles of polarimetric variables were observed to become more vertically homogeneous with time.

1. Introduction

Polarimetric radars provide the ability to differentiate between meteorological and nonmeteorological scatterers (Zrnić and Ryzhkov 1999), which facilitates the identification of tornadic debris (Ryzhkov et al. 2002, 2005). The tornadic debris signature (TDS) is characterized by low values of copolar cross-correlation coefficient ρ_{hv} , a local maximum in reflectivity factor Z_H , and low values in differential reflectivity Z_{DR} (Ryzhkov et al. 2002, 2005), often, but not always, collocated with a tornadic vortex signature (e.g., Van Den Broeke and Jauernic 2014). Tornadic debris signatures can be used operationally, with great caution, to confirm the presence of ongoing tornadoes (Schultz et al. 2012a,b; Snyder and Ryzhkov 2015). The focus of TDS research has broadened from tornado detection to include the relationship between the behavior of tornadic debris and tornado- and storm-scale kinematic processes. For example, longer-lived and more-intense tornadoes have been observed to have TDSs with larger volumetric coverage and TDSs that extend to higher altitudes than

 ${\it Corresponding\ author}. \ {\it Casey\ B.\ Griffin, casey.griffin@ou.edu}$

comparatively weaker tornadoes (Bodine et al. 2013; Van Den Broeke and Jauernic 2014; Van Den Broeke 2015). Many tornadoes with enhanced Fujita (EF)-scale ratings of EF-2 or less may not exhibit any TDS (Kumjian and Ryzhkov 2008; Van Den Broeke and Jauernic 2014). Bodine et al. (2013) found that large areas of debris fallout occur as tornadoes weaken and updrafts can no longer suspend as much debris. Consistent with the results of Bodine et al. (2013), Houser et al. (2016) found that as tornado intensity decreased, the areal coverage of the TDS at low levels increased, whereas at upper levels, the areal coverage decreased. The 24 May 2011 TDS for El Reno, Oklahoma, also exhibited vertically propagating wavelike bulges along its periphery, which may be indicative of centrifugal waves within the tornado (Houser et al. 2016). Stronger tornadoes often exhibit TDSs with higher values of Z_H , lower values of Z_{DR} , and lower values of $\rho_{\rm hv}$ (Bodine et al. 2013; Van Den Broeke 2015). Bodine et al. (2014) found that values of Z_H and ρ_{hv} were larger at S band within the TDS compared to at C band due to non-Rayleigh scattering effects and that the dualwavelength differences were larger when the tornado was producing more damage. Within the TDS,

DOI: 10.1175/MWR-D-19-0156.1

 Z_H was found to decrease with height and $\rho_{\rm hv}$ was found to increase with height, presumably because large, heavy debris is not lofted to as high of an altitude as light debris (Bodine et al. 2014).

In the near-tornado environment, comma-shaped appendages to the TDS could indicate the tornado interacted with the rear-flank downdraft (RFD), which ejected debris from within the tornado preferentially in one direction (Kurdzo et al. 2015). Appendages to the TDS could also be the result of light debris being lofted by convergent inflow into the tornado (Houser et al. 2016). Similarly, an extension to the TDS aloft, called a "debris overhang," could indicate a near-tornado updraft is suspending light debris that are falling out of the tornado (Wakimoto et al. 2015).

While many studies have focused on the near-tornado debris field, comparatively little research has explored the larger-scale transport and sedimentation of debris. Damage and debris surveys suggest that light debris are transported farther than heavy debris, while the majority of debris fall out to the left of the tornado track due to storm-relative wind shear (Snow et al. 1995). Trajectory calculations using a near-storm sounding confirm these previous observations (Magsig and Snow 1998) and provide insight into how debris can sediment in the rear flank, left flank, and forward flank of storms. Knox et al. (2013) confirmed that the majority of debris sediment to the left of the tornado track using the Hybrid Single-Particle Lagrangian Integrated Trajectory (HYSPLIT) model and a large dataset of debris items obtained from social media postings in the aftermath of the 27 April 2011 tornado outbreak. However, Knox et al. (2013) also found that the debris that were transported the farthest actually traveled to the right of tornado motion, perhaps due to being lofted to higher altitudes and experiencing more westerly winds. Van Den Broeke (2015) provided polarimetric radar observations of debris fallout both downstream of the storm-relative flow and on the northwest periphery of supercells. Fallout of debris has also been documented by polarimetric radar within the RFD in the wake of the tornado (Ryzhkov et al. 2005; Bodine et al. 2013). Additionally, lofted light debris and biological scatterers are often observed within storm inflow and along the rear-flank gust front (RFGF; e.g., Ryzhkov et al. 2005; Wakimoto et al. 2015). Much of this light debris may not have been lofted by the tornado, but rather by strong winds in the near-tornado environment. However, this debris may also be entrained into the TDS (Houser et al. 2016).

In this study, debris sedimentation within the 10 May 2010 Norman–Little Axe EF-4 tornado is analyzed using data collected by the University of Oklahoma's Polarimetric Radar for Innovations in Meteorology and Engineering (OU-PRIME) C-band radar (Palmer et al. 2011).

OU-PRIME's 0.45° beamwidth provides finescale observations of tornadic debris and enables a novel statistical comparison of debris characteristics within the tornado and debris in the near-tornado environment, which includes debris fallout from the tornado and debris lofted along the RFGF. This case provides a unique opportunity to compare TDS characteristics of two tornadoes in close proximity to one another. In addition to the Norman-Little Axe tornado, an EF-2-rated "landspout" tornado formed along the RFGF of the same parent supercell and eventually passed within a few kilometers of the Norman-Little Axe tornado. As previously discussed, tornadoes with different intensities broadly exhibit differences in TDS characteristics and behavior. In this instance, the two tornadoes encountered similar land cover for the analyzed period. Land cover modifies TDS properties through the scattering characteristics of debris available to be lofted (Van Den Broeke and Jauernic 2014; Van Den Broeke 2015); therefore, any differences in the two TDSs are likely due to tornado- and storm-scale processes. In addition to a comparison of the two TDSs, a novel dual-wavelength comparison of debris at C and S bands within the Norman-Little Axe tornado is performed. The dual-wavelength profiles of debris inside the tornado and outside the tornado are contrasted. Last, novel observations of the major axis of an elongated TDS rotating with height are presented.

2. Methods

a. Case overview

The 10 May 2010 tornado outbreak spawned 56 tornadoes in Oklahoma, including 36 in the Norman Weather Forecast Office's county warning area. Of interest to this study are two tornadoes in Cleveland County, Oklahoma, that occurred just after 2230 UTC (Fig. 1). The Norman-Little Axe tornado (red star) occurred from 2232 to 2259 UTC and was rated EF-4. It had a 35-km pathlength, ~2-km maximum damage width, caused 2 fatalities, and injured 22 additional people. The landspout tornado (blue star) associated with the Norman-Little Axe supercell formed at 2239 UTC and dissipated at 2259 UTC. It was rated EF-2 and caused 3 additional injuries. The landspout tornado had a pathlength of 27 km and a maximum damage width of 400 m. More details on the event can be found online (https://www.weather.gov/ oun/events-20100510) and in Palmer et al. (2011).

b. Radar data and dual-Doppler synthesis

Polarimetric radar data used for this project were collected by OU-PRIME, located near the National Weather Center in Norman, Oklahoma, and KOUN, which is located at Max Westheimer Airport in Norman (Fig. 1). OU-PRIME is a C-band radar with a 0.45° beamwidth and

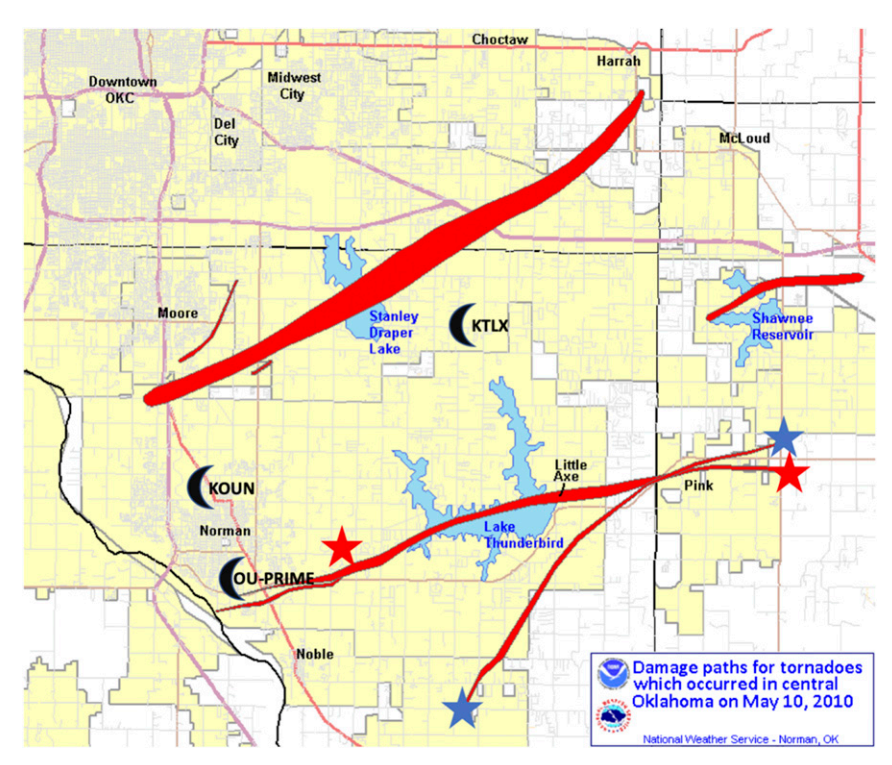


FIG. 1. Tornado damage paths in Cleveland County on 10 May 2010 [the figure is provided through the courtesy of the National Weather Service Office in Norman and is available online (https://www.weather.gov/oun/events-20100510-maps)]. The red stars indicates the track of the Norman–Little Axe tornado, and the blue stars indicates the track of the landspout tornado. The black crescents indicate the locations of the radars used in this study.

125-m gate length and is operated with a volumetric update time of 150s for the event. KOUN is an S-band radar with a 0.9° beamwidth and 250-m gate length and is operated with a 258- s update time during the event. Supplementary velocity data for dual-Doppler synthesis were collected by the KTLX WSR-88D instrument located just east of Oklahoma City, Oklahoma. At its closest range of 15 km to OU-PRIME, the Norman-Little Axe tornado was sampled as low as \sim 300 m above radar level (ARL) by OU-PRIME and as low as ~230 m by KOUN. Observations at both S and C band were qualitatively similar throughout the event [cf. Fig. 7 in Palmer et al. (2011)], with similar values of Z_H in precipitation. Larger values of Z_{DR} and lower values of ρ_{hv} were observed at C band in precipitation owing to non-Rayleigh scattering effects for large raindrops (e.g., Palmer et al. 2011). In regions of debris, Z_H was 10-15 dB higher at S band, with larger negative values of $Z_{\rm DR}$ and lower $\rho_{\rm hv}$ observed at C band owing to non-Rayleigh scattering. For light rain, values of Z_H were between 20 and 25 dBZ at both S and C band suggesting there

were no large differences in calibration for the two radars. Values of differential phase in the vicinity of the tornado ranged between -20° and 0° with initial differential phase near 0°. Vertically pointing "bird bath" scans were performed by OU-PRIME on the day of the event, resulting in a 0.1-dB correction in Z_{DR} for the dataset (Palmer et al. 2011). A scatterer-based calibration method similar to what was performed in Picca and Ryzhkov (2012) was used for KOUN. Values of Z_{DR} were approximately 0.1–0.2 dB in regions of ice hydrometeors (not shown), suggesting that appreciable calibration errors were not likely for this case. A simple differential attenuation correction calculation using the method outlined in Bringi et al. (1990) created no appreciable changes in the polarimetric fields (not shown). Thus, no differential attenuation correction was applied to the data. Additional details for the radar data used in this case can be found in Table 1 of Griffin et al. (2017), and further details regarding OU-PRIME and its observations during the event can be found in Palmer et al. (2011).

Radar data editing was completed using the NCAR Earth Observing Laboratory's Solo3 editing software (Oye et al. 1995). Clutter and multiple-trip echoes were subjectively removed, and manual dealiasing of velocity

¹The elevation angles included in the OU-PRIME volume coverage pattern were: 1°, 2°, 3°, 4°, 5°, 6.5°, and 9°.

data was performed. The data were also objectively thresholded on signal-to-noise ratio values below 0 dB. Dual-Doppler and objective analyses were performed using the Observation Processing and Wind Synthesis (OPAWS) code developed by D. Dowell (NOAA/ESRL) and L. Wicker (NSSL). The source code can be found online (http://code.google.com/p/opaws/). Radar data were objectively analyzed on a $30 \,\mathrm{km} \times 30 \,\mathrm{km}$ domain using a two-pass Barnes method (Barnes 1964) with a second-pass convergence parameter γ of 0.3 used to recover the amplitudes of smaller-scale spatial structures (Barnes 1973; Majcen et al. 2008). The limiting spatial resolution δ in the vicinity of the tornado ranged between approximately 225 and 375 m. A smoothing parameter $\kappa =$ $(1.33\delta)^2$] of 0.216 km⁻² (Pauly and Wu 1990) was chosen. A horizontal and vertical grid spacing of 250 m was chosen to accommodate coarser limiting spatial resolution in other parts of the analysis domain.² Motion of the supercell between each radar sweep in a volume was linearly corrected within the objective analyses prior to performing the dual-Doppler synthesis using a translation velocity determined by a comparison between the mesocyclone location at the previous time and its location at the analysis time.

In this study, dual-Doppler analyses are conducted at 2242 and 2247 UTC. For both of these analyses, the difference in low-level scan times between KTLX and OU-PRIME was ~20–40 s. Note that OU-PRIME and KTLX did not sample below 300 m in the vicinity of the tornado, which may lead to large errors in the vertical velocity estimates (Nolan 2013). However, vertical velocity is only used qualitatively in this study.

c. Debris classification

Originally, the proposed criteria for a TDS at S band were values of $Z_H > 45\,\mathrm{dB}Z$, $Z_\mathrm{DR} < 0.5\,\mathrm{dB}$, and $\rho_\mathrm{hv} < 0.8$ collocated with a vortex signature in radial velocity V_r (Ryzhkov et al. 2005). The criteria for Z_H were relaxed by Schultz et al. (2012a) to 30 dBZ and were further relaxed by Van Den Broeke and Jauernic (2014) to 20 dBZ given the Warning Decision Training Division (WDTB 2013) recommendation based on numerous tornadic events exhibiting $Z_H < 30\,\mathrm{dB}Z$. For this case, to capture lower debris concentrations within the weak-echo hole (WEH) and elsewhere outside the tornado at C band, a 10-dBZ threshold for tornadic debris was implemented, similar to what was used in Griffin et al. (2017) for this same event. An upper ρ_hv threshold of 0.82 was used based on the Bodine et al. (2013) finding of increasing

contribution of precipitation above this threshold. No $Z_{\rm DR}$ threshold was imposed to include resolution volumes for which debris and precipitation were both present. Because no $Z_{\rm DR}$ threshold was imposed and such a low $Z_{\rm H}$ threshold was used, the classification was manually checked to ensure that volumes dominated by biological scatterers with low $\rho_{\rm hv}$ and $Z_{\rm DR} > 5\,{\rm dB}$ were not misclassified as debris.

Debris in and near the Norman-Little Axe tornado was separated into "inner" and "outer" debris on the basis of whether resolution volumes (approximately $175 \,\mathrm{m} \times 175 \,\mathrm{m} \times 125 \,\mathrm{m}$ in azimuth \times elevation \times range for OU-PRIME in the vicinity of the Norman-Little Axe tornado at 2242 UTC) were within 1 km of the subjectively identified tornado center or between 1 and 3km from the tornado center. Tornado centers were determined using Doppler velocity couplets (not shown),³ with the WEH also used to guide these decisions for the Norman-Little Axe tornado.4 The inner debris classification can be thought of as a traditional TDS since the debris are collocated with the tornado vortex. The 1-km threshold was chosen because it approximately represents the radius of the maximum damage swath in this tornado during the analysis period. Outer debris is a combination of debris falling out of the tornado, debris lofted by inflow into the tornado, and debris lofted along the gust front near the tornado. The 3-km maximum radius for outer debris was chosen to prevent debris associated with the landspout tornado from being erroneously identified as debris falling out of the Norman-Little Axe tornado. In a few instances, debris are separated into "light" versus "heavy" debris classifications based on a subjective threshold of 30 dBZ, which was approximately the median value of OU-PRIME Z_H for debris at 1° elevation. Examples of the debris classification can be seen in Figs. 2j–1. These classifications can be thought of as a combination of debris size and concentration contributing to the magnitude of Z_H .

3. Results

a. OU-PRIME polarimetric and dual-Doppler observations of tornadic debris

At 2242 UTC, the Norman–Little Axe tornado had already been in progress⁵ for 10 min. At this time, the tornado

 $^{^2}$ We used the formula for grid spacing ($\Delta=\delta/2.5)$ from Koch et al. (1983) where values of δ exceeded 600 m in parts of the analysis domain.

 $^{^3}$ The tornado location on the ground may have differed slightly from these centers as a result of tornado tilt in the lowest $\sim\!250\,\mathrm{m}.$

⁴The landspout tornado did not exhibit a WEH.

⁵OU-PRIME was operating in a sector-scanning mode. Prior to 2242 UTC it was collecting data on the Moore–Choctaw tornado (Griffin et al. 2017) and not scanning the Norman–Little Axe tornado.

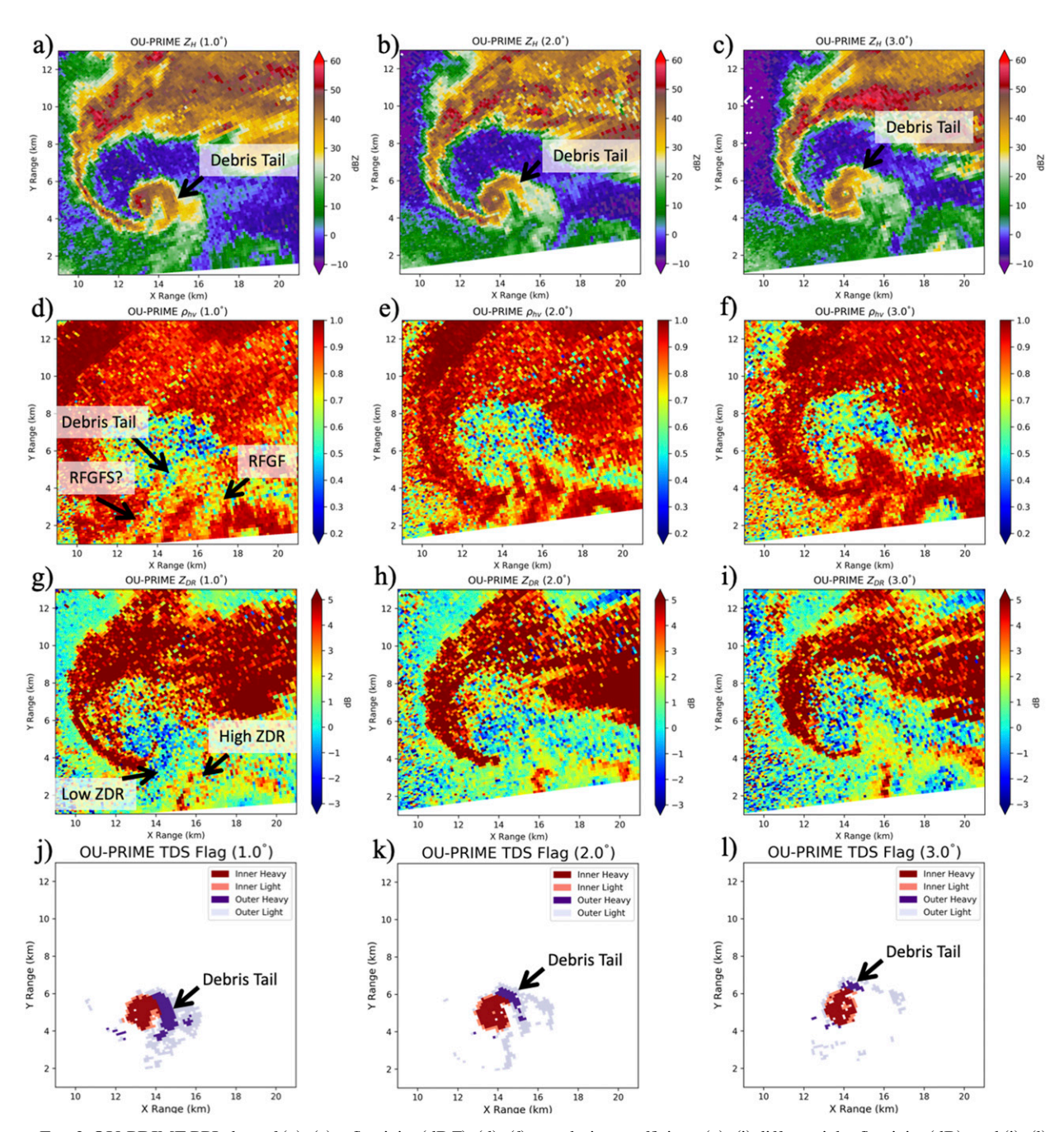


FIG. 2. OU-PRIME PPI plots of (a)–(c) reflectivity (dBZ), (d)–(f) correlation coefficient, (g)–(i) differential reflectivity (dB), and (j)–(l) debris classification at (left) 1.0° (~275 m ARL at the location of the Norman–Little Axe tornado), (center) 2.0° (~525 m ARL), and (right) 3.0° (~775 m ARL) elevation for the Norman–Little Axe tornado (western TDS only) valid at 2242 UTC. Ranges plotted here and elsewhere are relative to the location of OU-PRIME. In (d), RFGFS indicates the location of a possible rear-flank gust front surge. In (j)–(1), light and heavy are < 30- and > 30-dBZ Z_H , respectively.

exhibited a TDS with a 1.5-km diameter and a large appendage of debris extending to the east and south from the northeast side of the TDS (Fig. 2). This "tail" of debris became shorter and rotated counterclockwise with height (Figs. 2j–l), suggesting either that debris was not being lofted as high in the southern part of the debris tail, or

that debris was being transported toward the tornado with height. Dual-Doppler winds in the northern portion of the debris tail (Figs. 3a,c) indicated westward storm-relative winds, supporting the hypothesis that debris in the northern part of the tail was being ingested into the inner debris region in Figs. 2j-1.

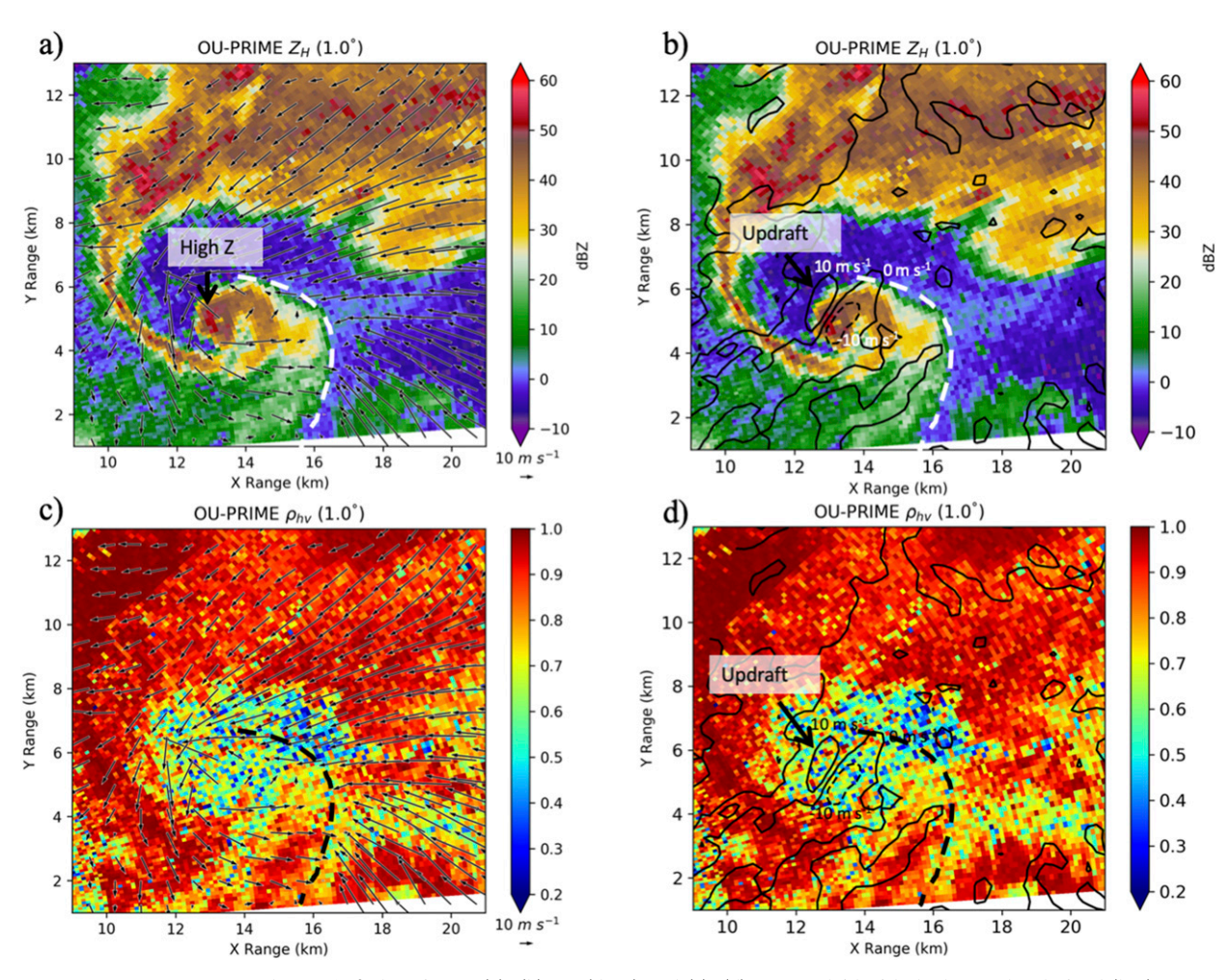


FIG. 3. OU-PRIME PPI plots at 1.0° elevation of (a), (b) Z_H (dBZ) and (c), (d) ρ_{hv} overlaid with dual-Doppler-derived (left) storm-relative horizontal winds (arrows) and (right) vertical velocity contoured at 10 m s⁻¹ intervals (dashed contours indicate negative vertical velocities) at 250 m ARL valid at 2242 UTC.

However, because there was approximately 20 s between each elevation scan, the shortening of the debris tail could also have been due to temporal changes in the debris field rather than to vertical changes in the debris field.

The debris tail appeared to be part of a larger linear region of low OU-PRIME $\rho_{\rm hv}$ extending to the south of the tornado. Another line of low $\rho_{\rm hv}$ was present to the east of the tornado and was collocated with the RFGF in the dual-Doppler analyses (Fig. 3a). While the dual-Doppler analyses did not show a secondary gust front associated with the debris tail, there may have been a shallow or underresolved feature, such as a rear-flank gust front surge, that was responsible for ejecting the debris to the east similar to what was seen in Kurdzo et al. (2015). OU-PRIME $Z_{\rm DR}$ along the RFGF was positive, whereas $Z_{\rm DR}$ within and extending southward from the debris tail was negative (Fig. 2g) suggesting different types or

orientations of scatterers along each of the linear features. Likely, light debris and insects were concentrated along the RFGF and the debris tail was made up mostly of debris.

At 1° elevation, the highest Z_H and most negative $Z_{\rm DR}$ within the TDS were on the west side of the tornado (Figs. 2a,g). Dual-Doppler-derived vertical velocities (Fig. 3b) were most positive on the west side of the tornado, which may indicate that enhanced debris lofting occurred in this region. A small WEH was present throughout the entire observed depth of the storm and became larger with height, suggesting debris and hydrometeors were being centrifuged from the tornado (Dowell et al. 2005).

Aloft, a large band of mostly likely small drops with low, yet positive $Z_{\rm DR}$ and high $\rho_{\rm hv}$ (Fig. 4) was present to the south and southeast of the TDS (Kumjian 2011; French et al. 2015). Small drops began to fill in the

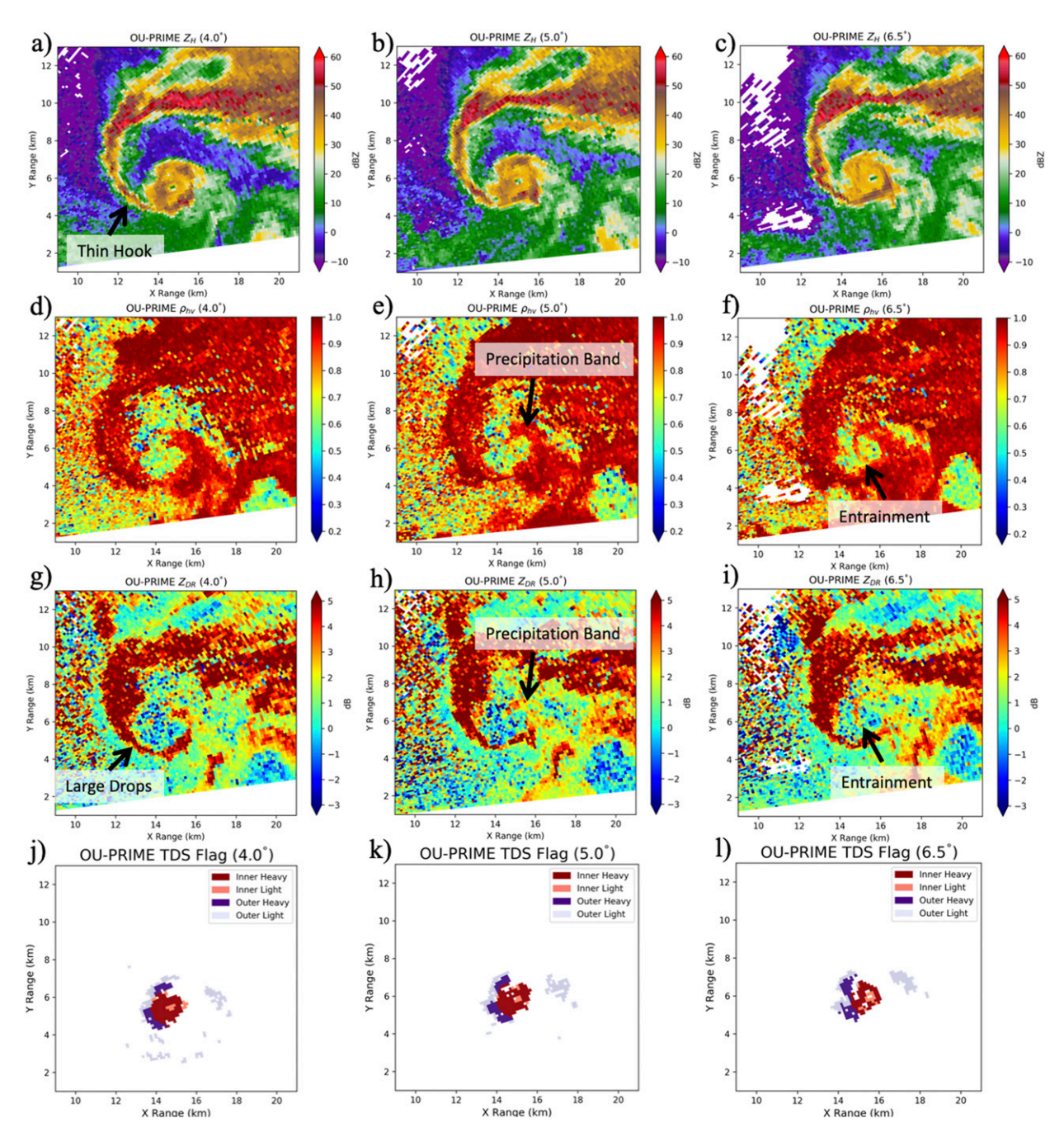


FIG. 4. As in Fig. 2, but at (left) 4.0° (\sim 1075 m ARL), (center) 5.0° (\sim 1325 m ARL), and (right) 6.5° (\sim 1725 m ARL) elevation valid at 2242 UTC.

area of inflow to the northeast of the tornado at 5.0° and 6.5° (Figs. 4e,f). A very narrow band of most likely large raindrops nearly encompassed the TDS. At 5.0° and 6.5° elevation, a narrow band of precipitation with moderately high values of $Z_{\rm DR}$ wrapped into the TDS (Figs. 4h,i). The moderate values of $Z_{\rm DR}$ suggest that the band may have been composed of a mixture of large drops and debris. The entrainment of

large drops could potentially raise the values of $Z_{\rm DR}$ and $\rho_{\rm hv}$ throughout the entire TDS even when they are not the dominant scatterers (Bodine et al. 2014). Unlike at lower levels, nearly all resolution volumes containing debris at upper levels exhibited $Z_H > 30\,{\rm dB}Z$ (Figs. 4j–l). This may be because regions of debris with $Z_H < 30\,{\rm dB}Z$ at low levels had smaller vertical velocities (Figs. 2j–l). Bulk TDS statistical

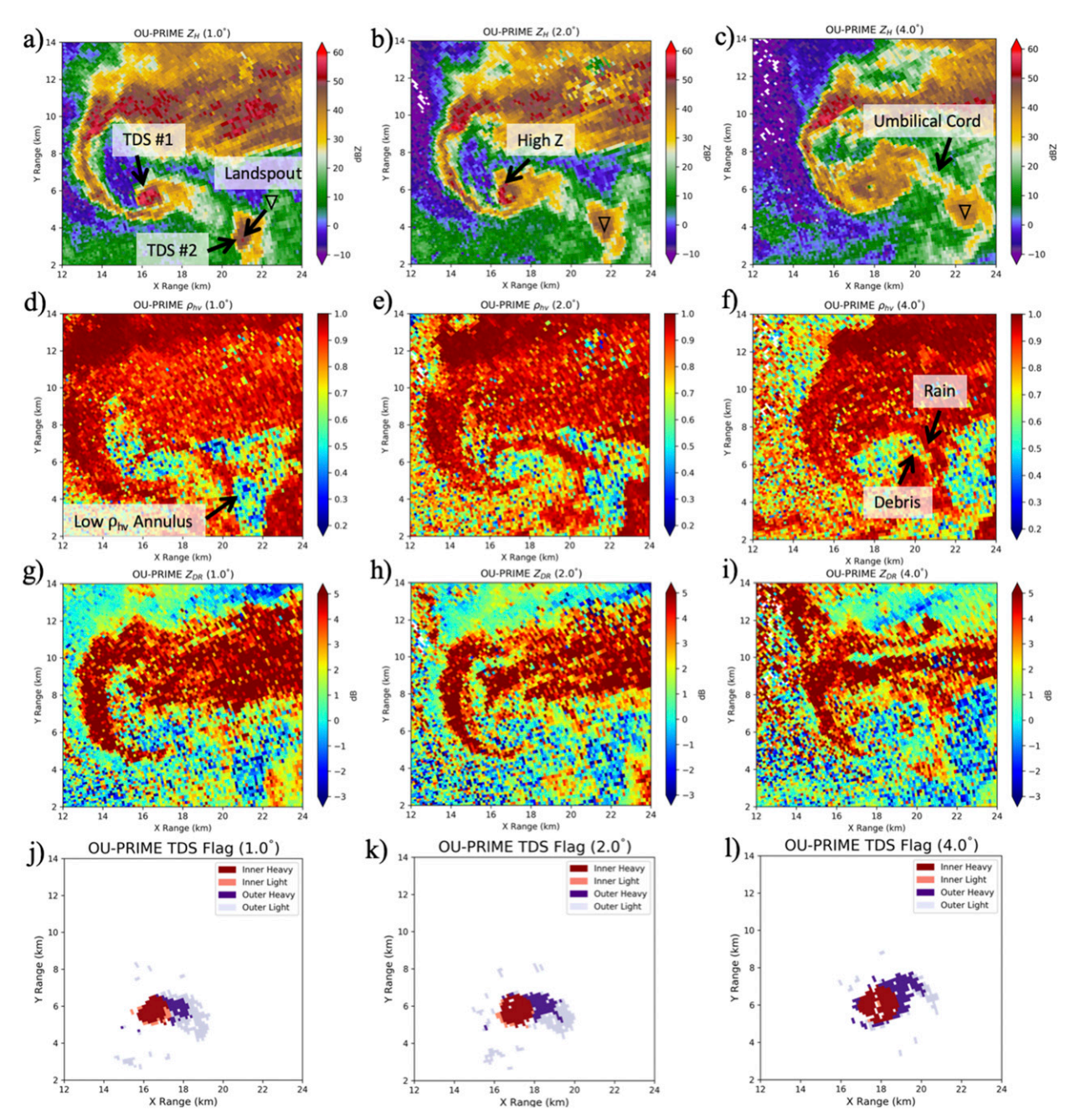


Fig. 5. As in Fig. 2, but at (left) 1.0° (\sim 325 m ARL), (center) 2.0° (\sim 625 m ARL), and (right) 4.0° (\sim 1300 m ARL) elevation valid at 2244 UTC. Triangles indicate the position of the landspout tornado.

properties will be a subject of discussion in the next two subsections.

b. Comparison of simultaneous TDSs using OU-PRIME

At 2244 UTC, a landspout tornado located along the RFGF to the east of the Norman–Little Axe tornado entered OU-PRIME's observation domain 5 min after

tornadogenesis (TDS 2 in Fig. 5a). The eastern TDS was elongated such that the major axis was along the gust front with a north-south orientation. The landspout tornado did not exhibit a WEH, although this could be because the diameter was too small to be resolved so far from the radar. An annulus of low ρ_{hv} (Fig. 5d) was present in the eastern TDS, similar to what was observed in the Moore, Oklahoma, tornado on this same day

(Griffin et al. 2017); however, it is unlikely this was associated with large tornado subvortices like were observed in the Moore tornado near its RMW. Meanwhile, the Norman–Little Axe (western) TDS still exhibited a well-defined WEH and was elongated such that the major axis was oriented east–west, which paralleled the local RFGF orientation in the dual-Doppler analyses performed before (Fig. 3) and after this time (Fig. 7). Similar to the previous time, a region of debris with <30-dBZ Z_H extended to the east of the Norman–Little Axe tornado. However, at higher elevations nearly all of the resolution volumes containing debris exhibited $Z_H > 30\,\mathrm{dBZ}$ (Figs. 5j–l).

Aloft at 4°, the eastern TDS exhibited slightly lower Z_H compared to at low levels and had a much larger area than in the low levels (Figs. 5c,f,i,l). The TDS extended well to the north of the location of the tornado, with the northern portion of the TDS having relatively low Z_H while maintaining similar values of $Z_{\rm DR}$ and $\rho_{\rm hv}$ as the rest of the TDS. Perhaps this was the result of smaller concentrations of debris being advected to the north and ingested by the storm-scale updraft. A similar elongation of the Norman–Little Axe TDS to the northeast was also observed at this time (Fig. 5f). In addition to the northeast extension of the Norman–Little Axe TDS, a northwest–southeast-oriented appendage to the TDS was also present at 4° elevation on its northeast side (Fig. 5f).

At 2247 UTC, the landspout tornado had moved north and west in a storm-relative sense and was less than 5 km from the Norman–Little Axe tornado (Fig. 6). At this time, the Norman-Little Axe tornado still had a WEH, whereas the landspout tornado had the highest Z_H at its center and decreasing Z_H with radius outward (Fig. 6a). An area of debris with >30-dBZ Z_H extended to the east of the Norman-Little Axe tornado (Fig. 6j). This region of debris increased in Z_H with height while maintaining a similar shape and area (Fig. 61), perhaps as a result of large amounts of debris that were previously within the tornado being redistributed eastward. The landspout TDS exhibited two appendages, one on its northwest side and one on its southeast side. Dual-Doppler analyses (Fig. 7) suggest that the southeastern appendage was associated with inflow into the tornado along the RFGF similar to the sawtooth features observed by Houser et al. (2016). It is likely that this appendage was made up of lighter debris lofted along the gust front and ingested into the tornado by strong inflow. Conversely, the appendage on the northwest side of the TDS was associated with outflow from the tornado and was likely composed of debris lofted by and ejected from the tornado, similar to what was documented by Kurdzo et al. (2015).

Differential reflectivity less than $-2\,\mathrm{dB}$ was observed in the northwest portion of the landspout TDS (Figs. 6g and 7c). Past studies (e.g., Ryzhkov et al. 2005; Bluestein et al. 2007; Griffin et al. 2017; Umeyama et al. 2018; Wakimoto et al. 2018) have hypothesized that this negative Z_{DR} is the result of common debris alignment. Consistent with the observations of Griffin et al. (2017) and Wakimoto et al. (2018), the negative Z_{DR} was observed at the periphery of the tornado, perhaps where tangential velocities were much larger than vertical velocities (Umeyama et al. 2018).

Statistical analyses of OU-PRIME data were conducted to compare the polarimetric characteristics of the two TDSs at 2244 and 2247 UTC using the criteria in section 2b. Median OU-PRIME Z_H at 1° elevation for debris volumes in the Norman-Little Axe tornado was 5–9 dB higher than in the landspout tornado (Fig. 8a). In the landspout tornado, median Z_H decreased slightly with height, whereas median Z_H was relatively constant with height in the Norman-Little Axe tornado. However, these observations were all above 300 m ARL, below which the largest decrease in Z_H typically occurs (e.g., Wurman et al. 1996; Dowell et al. 2005; Wakimoto et al. 2018). Ninetieth-percentile Z_H was approximately 7 dB higher in the Norman-Little Axe tornado than the landspout tornado, and in both tornadoes 90thpercentile Z_H decreased with height. This suggests that the fallout rate of the largest debris was greater than for smaller debris, which is consistent with physical expectations and similar to observations by Bodine et al. (2014). Both tornadoes were interacting with broadly similar land cover, so therefore the differences in median and 90th-percentile Z_H between tornadoes are more likely attributed to differences in tornado intensity rather than land cover (Bodine et al. 2013; Van Den Broeke and Jauernic 2014; Van Den Broeke 2015). The Norman-Little Axe tornado produced EF-4 damage and likely lofted larger and greater quantities of debris than the EF-2 landspout tornado. Additionally, differential velocity ΔV in the Norman-Little Axe tornado was $\sim 15-25 \,\mathrm{m\,s^{-1}}$ higher than in the landspout tornado (Fig. 9). However, the tornadoes were more than 20 km away from the radars and the lowest ~300 m were not

⁶The narrower beamwidth of OU-PRIME means that it captures greater spatial variability in the polarimetric variables than does KOUN, which may broaden the bulk distribution of polarimetric variables within the TDS. Although the median values are likely not affected by the differences in spatial sampling, the 90th-percentile values may be slightly larger at C band than they would have been given similar resolution volume size.

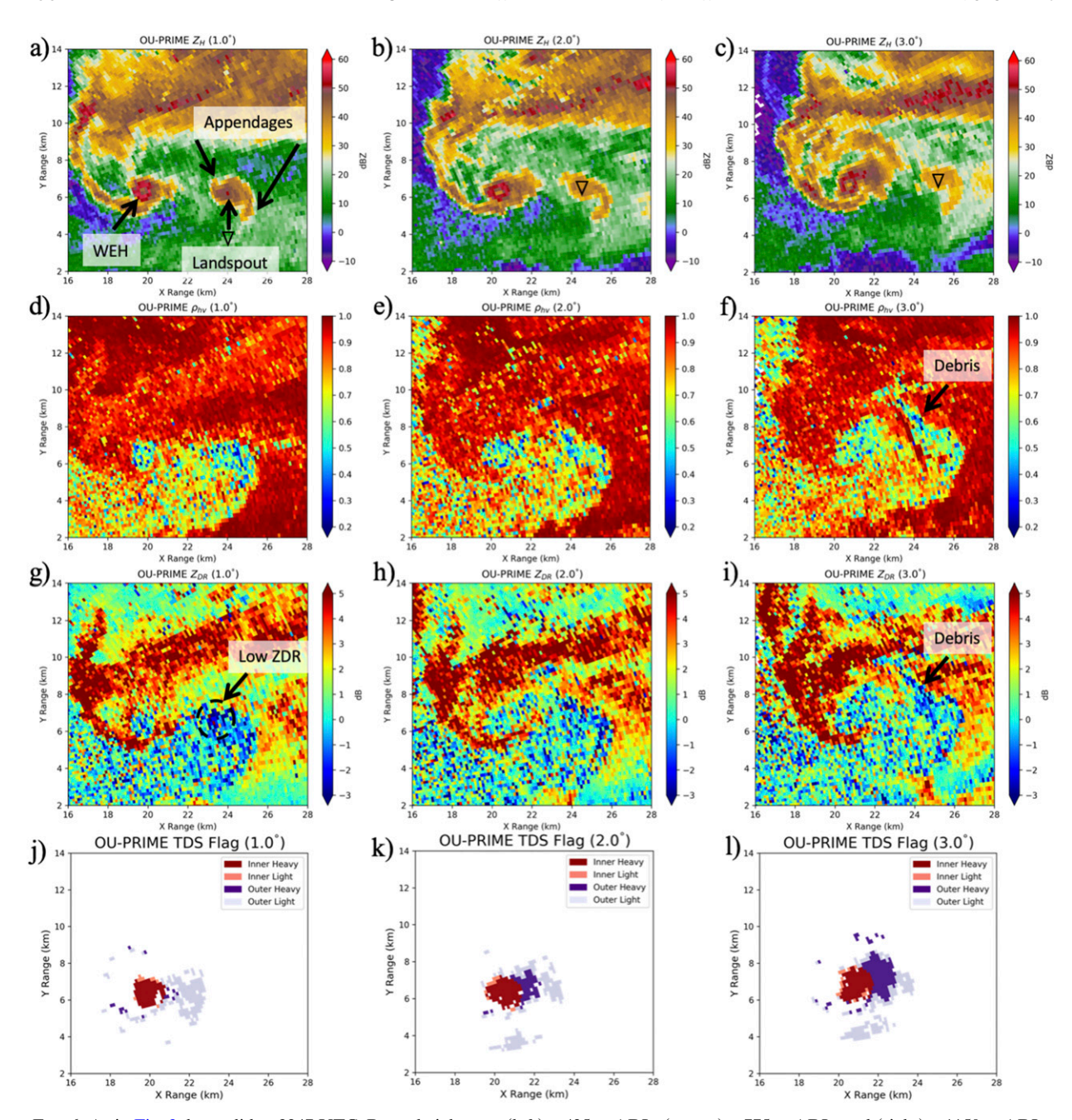


FIG. 6. As in Fig. 2, but valid at 2247 UTC. Beam heights are (left) ~425 m ARL, (center) ~775 m ARL, and (right) ~1150 m ARL.

sampled, so the absolute values of ΔV as a proxy for tornado intensity should be used with caution.

It is possible debris lofted 5–10 min prior to the first analysis time when the Norman–Little Axe tornado was encountering a more urban area were still present within the TDS. This difference in land cover would introduce some variance in the types of scatterers present within the two tornadoes. However, this is at least partially mitigated by the fact that both the Norman–Little Axe

tornado and landspout tornado encountered man-made structures late in the analysis period near Little Axe. Additionally, the Norman-Little Axe tornado passed over a lake between 2244 and 2247 UTC, which may have altered TDS characteristics for a brief period between analysis times.

Median and 90th-percentile OU-PRIME $Z_{\rm DR}$ for tornadic debris were approximately 0.5–1.0 dB higher in the Norman–Little Axe tornado than the landspout

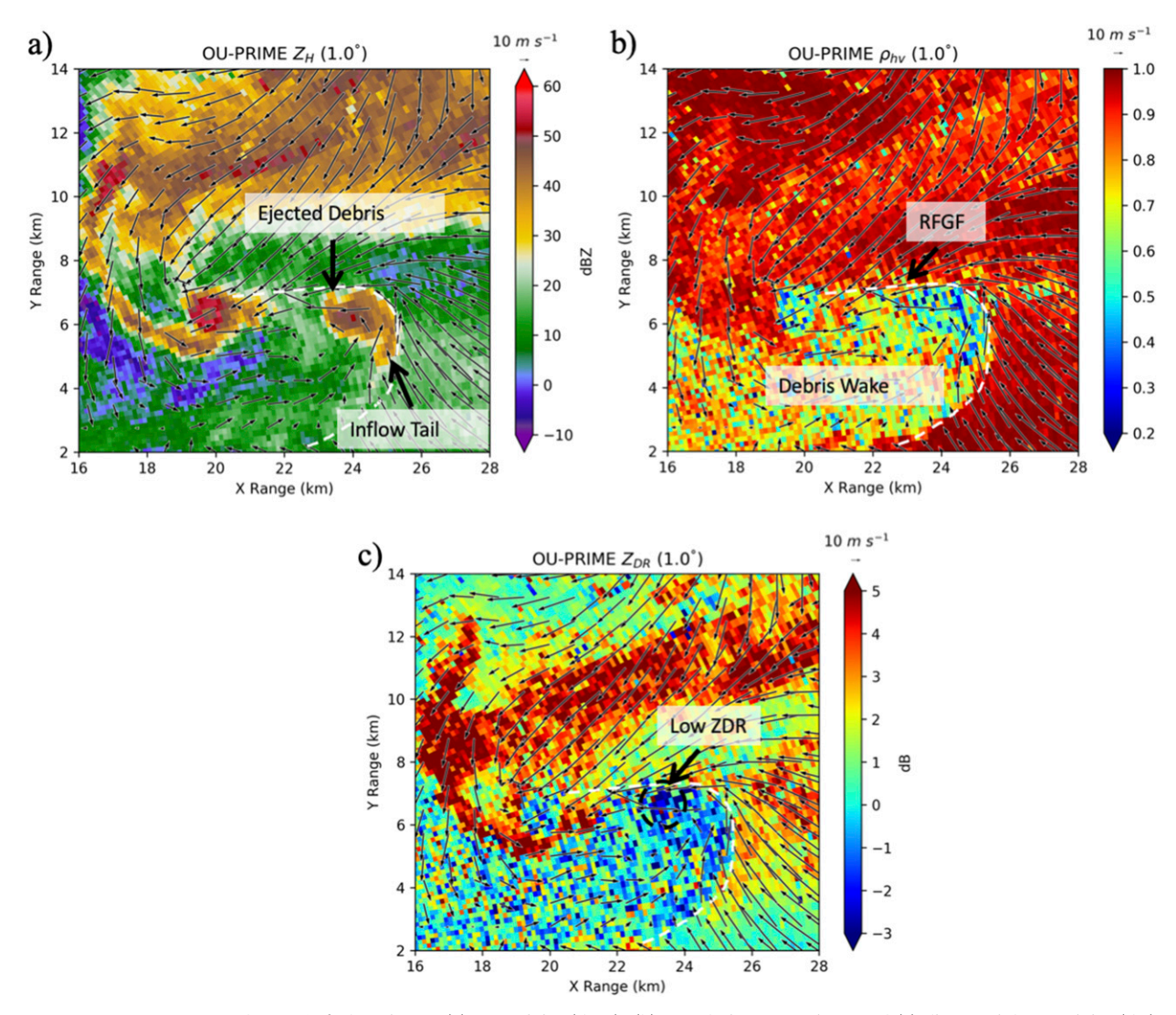


FIG. 7. OU-PRIME PPI plots at 1.0° elevation of (a) reflectivity (dBZ), (b) correlation coefficient, and (c) differential reflectivity (dB) overlaid with dual-Doppler-derived storm-relative horizontal winds (arrows) at 250 m ARL valid at 2247 UTC.

tornado (Fig. 8b). For both tornadoes, median Z_{DR} increased slightly with height and 90th-percentile $Z_{\rm DR}$ exhibited no appreciable trend. Median and 10th-percentile ρ_{hv} were approximately 0.05 higher in the Norman-Little Axe tornado, and for both tornadoes median and 10th-percentile ρ_{hv} increased with height (Fig. 8c). The increase in ρ_{hv} coupled with the decrease in Z_H with height is likely due to the fallout and centrifuging of the largest scatterers as altitude increases (Bodine et al. 2014). Precipitation entrainment may also have been responsible for the higher $Z_{\rm DR}$ as well as the higher $\rho_{\rm hv}$ in the Norman-Little Axe tornado, similar to what was observed in Bodine et al. (2014). While differences in the magnitudes of polarimetric variables exist because of differences in tornado intensity and precipitation entrainment, the

behavior of the vertical profiles of polarimetric variables within the two tornadoes was similar.

c. Debris sedimentation

In an effort to understand how tornadic debris are dispersed into adjacent updraft and downdraft regions, the areal extent of debris was calculated in each quadrant relative to the tornado's position in order to quantify the distribution of debris with height. In the low levels, the majority of the near-tornado debris field for the Norman–Little Axe tornado was located to the east of the tornado center (Fig. 10a). Comparatively little debris was located to the north and south of the tornado, with nearly no debris located to the west of the tornado other than debris within the annulus of high reflectivity that surrounded the WEH. The area of debris located to

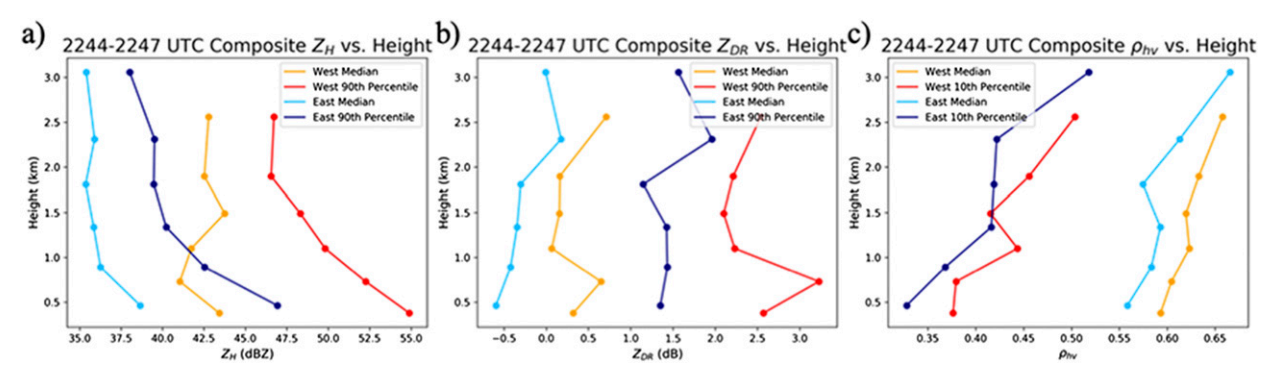


FIG. 8. Composite profiles of OU-PRIME (a) reflectivity (dBZ), (b) differential reflectivity (dB), and (c) correlation coefficient vs height (km) valid from 2244 to 2247 UTC. Red lines indicate the profiles of the western tornado, and blue lines indicate the profiles of the eastern tornado. Light colors represent median values, and dark colors represent 90th-percentile values.

the east of the tornado center decreased significantly with height from an average of $3.5 \,\mathrm{km^2}$ at 1.0° to less than $1 \,\mathrm{km^2}$ at 6.5° . The area of debris to the south of the tornado remained relatively constant up to 4.0° ($\sim 1.5 \,\mathrm{km}$ ARL) before it decreased slightly at 5.0° ($\sim 2 \,\mathrm{km}$ ARL) and 6.5° ($\sim 2.75 \,\mathrm{km}$ ARL) elevation. In contrast, the areal extent of debris to the north and

west of the tornado increased with height up to 5.0° before decreasing slightly at 6.5°, likely as a result of an overall decrease in total debris area at higher elevations.

Apart from the first observation time, the total area of debris with >30-dBZ Z_H lofted near the Norman–Little Axe tornado increased with height (Fig. 10b). It is likely

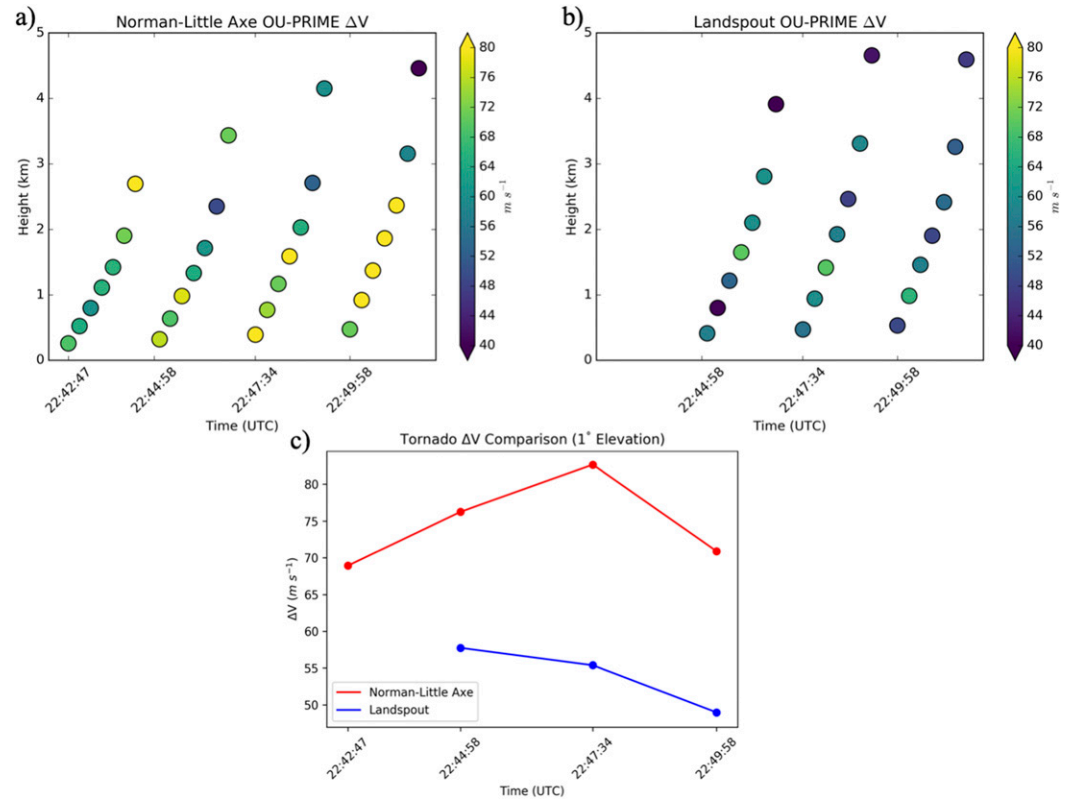


FIG. 9. Time-height analyses of OU-PRIME differential velocity (color fill; $m \, s^{-1}$) for (a) the Norman–Little Axe tornado and (b) the landspout tornado. (c) A comparison of differential velocity ($m \, s^{-1}$) for the two tornadoes at 1° elevation.

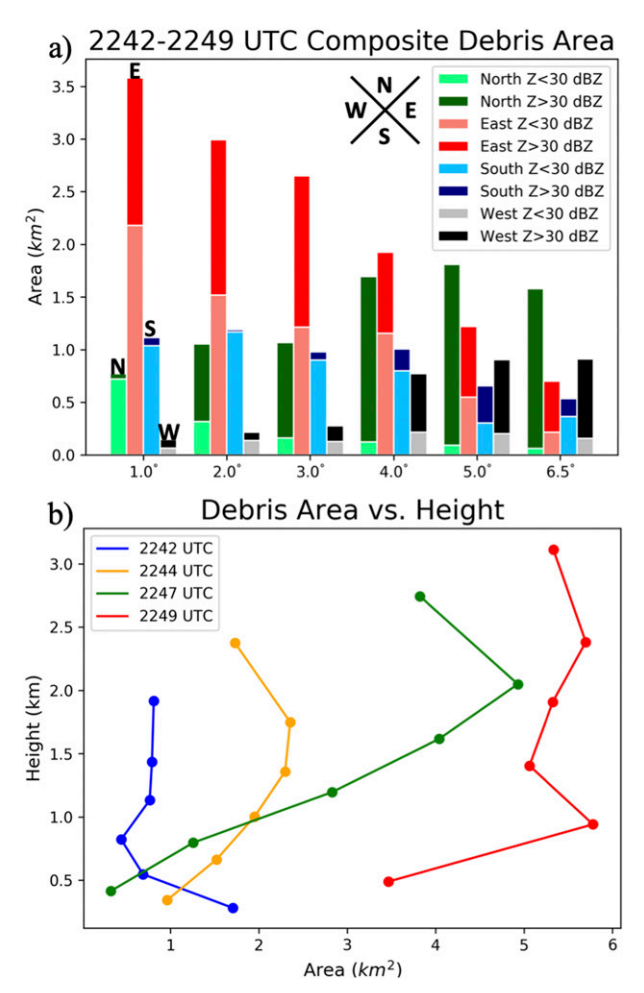


FIG. 10. (a) OU-PRIME areal extent (km²) of debris at 1.0°, 2.0°, 3.0°, 4.0°, 5.0°, and 6.5° in the northern (green), eastern (red), southern (blue), and western (black) quadrants of the Norman–Little Axe TDS. Quadrants are defined relative to the center of the tornado. Dark colors represent area with reflectivity $> 30 \, \text{dBZ}$, and light colors represent area with $< 30 \, \text{dBZ}$ reflectivity. (b) Area (km²) of debris exhibiting $Z_H > 30 \, \text{dBZ}$ vs height (km) valid at 2242 UTC (blue line), 2244 UTC (orange line), 2247 UTC (green line), and 2249 UTC (red line).

that the change in the vertical distribution of debris after 2242 UTC was due to the increased centrifuging of debris associated with an increase in ΔV between 2242 and 2247 UTC (Fig. 9a). Debris would have been more likely to detrain farther from the tornado when tornado intensity was greater (Wakimoto et al. 2011). In addition to greater debris centrifuging, the increase in tornado intensity likely caused an increase in vertical debris flux (Batt et al. 1999), which would have resulted in the observed increase in the total volume of lofted debris.

The large area of debris to the east of the tornado in the low levels was largely due to the aforementioned debris tail to the east of the Norman–Little Axe tornado

(e.g., Figs. 5a,d,g,j). As previously discussed, the debris tail decreased in length and areal extent with height, which was one reason why the area of debris to the east of the tornado decreased with height. However, another factor in the upward decrease in area of debris to the east of the Norman-Little Axe tornado was the counterclockwise rotation of the TDS with height (Fig. 11). At 2247 UTC, the major axis of the TDS was oriented nearly east-west (Figs. 11a,d,g). At increasing elevations, the major axis of the TDS rotated to the east-northeast (Figs. 11b,e,h) and then to the northeast (Figs. 11c,f,i). The TDS also became elongated as debris were transported to the north by storm relative winds (not shown). From these observations it can be concluded that the areal extent of debris to the north of the tornado grew at the expense of the area of debris to the east of the tornado. This redistribution of debris to the north of the tornado is a near-real-time polarimetric radar verification of the observations that the majority of debris is redistributed to the left of the tornado track (Snow et al. 1995; Magsig and Snow 1998).

At 2249 UTC, the Norman–Little Axe TDS maintained a northeastward orientation above the 4.0° elevation scan (Fig. 12). The Norman–Little Axe TDS became increasingly elongated with height, extending approximately 4 km along its major axis at 6.5° elevation (Figs. 12c,f,i,l). As noted at previous times, virtually all resolution volumes containing debris within the Norman–Little Axe tornado aloft exhibited $Z_H > 30 \, \mathrm{dB}Z$ (Figs. 12j–l).

Dual-Doppler-derived, mean storm-relative wind within $3\,\mathrm{km}$ of the Norman–Little Axe tornado at 2247 UTC veered with height (Fig. 13). In the low levels, mean storm relative flow was to the south, largely influenced by northerly winds within the RFD and east-northeasterly inflow into the tornado (Fig. 7). However, the mean storm relative winds shifted to the northeast with height (Fig. 13) with mean winds of $\sim\!20\,\mathrm{m\,s^{-1}}$ to the northeast at $3.75\,\mathrm{km}$ ARL, approximately the altitude of the TDS at 6.5° elevation in Figs. 14c, 14f, 14i, and 14l 2 min later at 2249 UTC. It is likely that the veering storm-relative wind profile was responsible for the rotation and elongation of the TDS to the northeast with height.

d. Dual-wavelength observations of inner versus outer debris using OU-PRIME and KOUN

Dual-wavelength differences provide information on debris characteristics (e.g., size) that are independent of debris concentration and may provide information needed for future Doppler velocity bias correction (e.g., Wakimoto et al. 2012; Nolan 2013; Bodine et al. 2014; Umeyama et al. 2018). For the Norman–Little Axe

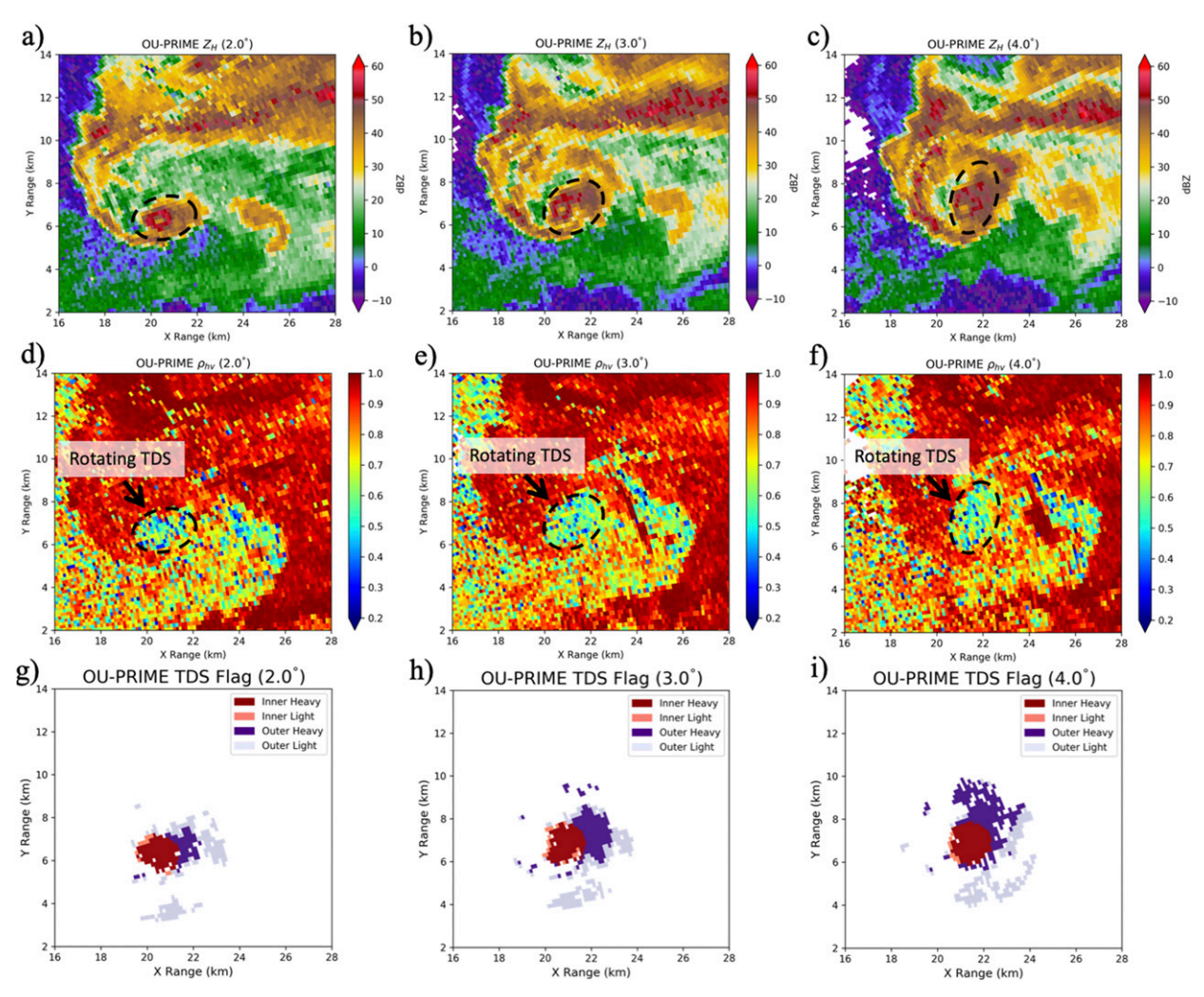


FIG. 11. OU-PRIME PPI plots of (a)–(c) reflectivity (dBZ), (d)–(f) correlation coefficient, and (g)–(i) Norman–Little Axe tornado debris classification at (left) 2.0° (\sim 775 m ARL), (center) 3.0° (\sim 1150 m ARL), and (right) 4.0° (\sim 1575 m ARL) elevation valid at 2247 UTC.

tornado, the profiles of inner debris within 1 km of the tornado, and outer debris between a 1- and 3-km radius from the tornado were compared at C and S bands (Fig. 14). At low levels, Z_H was higher for inner debris than for outer debris (Figs. 14a,d). As previously discussed, Z_H decreased slightly with height for inner debris at both wavelengths. However, for outer debris, Z_H increased with height with median and 90th-percentile values at S and C bands becoming similar to their respective values for inner debris at 6.5° elevation. This occurred because larger debris were centrifuged outward and advected northward away from the center of the tornado (e.g., Fig. 11). Histograms of Z_H (not shown) confirm that the distribution of Z_H for outer debris at 6.5° was very similar to the distribution for inner debris at 1.0° for both wavelengths. Additionally,

the size distribution of debris likely narrowed with height due to the fallout of large debris causing more similar values of Z_H between inner and outer debris at higher elevations.

Median and 90th-percentile Z_H were approximately 7 dB higher at S band than at C band for inner debris. This was likely because volumes of inner debris were more likely to contain larger scatterers, which remain Rayleigh scatterers for larger sizes at S band than C band resulting in higher Z_H [cf. Fig. 3 in Bodine et al. (2016)]. The dual-wavelength difference in Z_H at low levels for outer debris was comparatively small with 1–2-dB differences in median and 90th-percentile Z_H below 1000 m ARL, likely because the debris sizes were much smaller for outer debris. The dual-wavelength difference in Z_H for outer debris became greater above 1 km

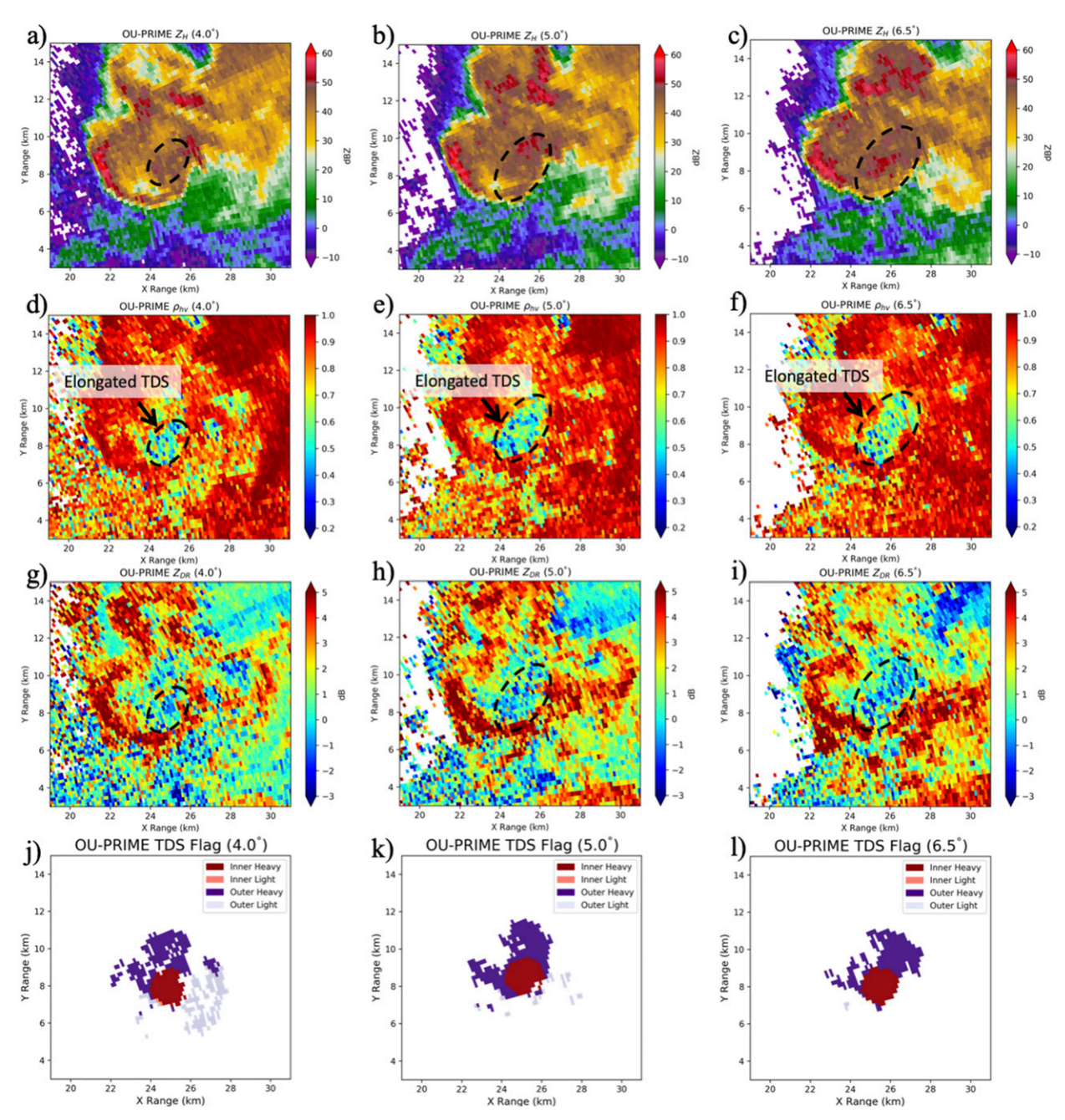


FIG. 12. As in Fig. 2, but at (left) 4.0° (\sim 1825 m ARL), (center) 5.0° (\sim 2275 m ARL), and (right) 6.5° (\sim 3050 m ARL) elevation valid at 2249 UTC.

and more similar to the dual-wavelength difference for inner debris, going from an \sim 3-dB mean difference below 1 km to an \sim 9-dB mean difference between 1 and 2 km as larger debris particles were redistributed away from the tornado.

Median and 10th-percentile ρ_{hv} were larger at S band than at C band (Fig. 14c) for inner debris. This is consistent with the findings of Bodine et al. (2014) and is due to a greater impact of resonance effects at C band resulting

from a larger proportion of non-Rayleigh scatterers in a given volume containing debris. Additionally, C band is more sensitive to nonspherical shapes (Balakrishnan and Zrnić 1990), which lowers $\rho_{\rm hv}$. At both S and C bands, $\rho_{\rm hv}$ increased with height for inner debris, likely due to the fallout of larger debris and consistent with the observations of Bodine et al. (2014). Conversely, differences in S- and C-band $\rho_{\rm hv}$ were minimal for outer debris while median and 10th-percentile values of $\rho_{\rm hv}$ remained relatively

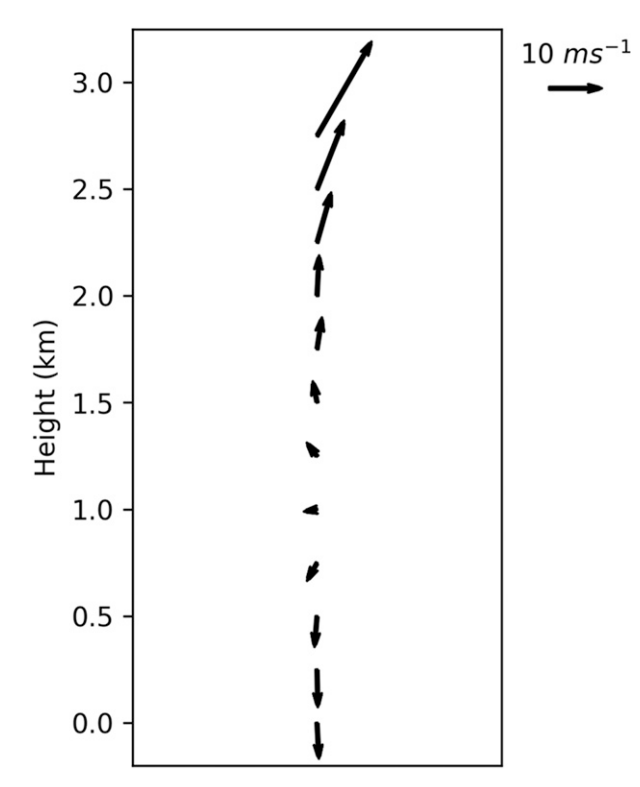


FIG. 13. Dual-Doppler-derived mean storm relative horizontal wind profile, computed within a 3-km radius of the Norman–Little Axe tornado valid at 2247 UTC.

constant with height in the lowest 2.5 km ARL (Fig. 14f). The smaller dual-wavelength differences in both ρ_{hv} and Z_H support the hypothesis that, in general, outer debris was comparatively smaller than inner debris. Additionally, both median and 10th-percentile ρ_{hv} were 0.1 higher for outer debris than inner debris, suggesting proportionally fewer non-Rayleigh scatterers in the outer region. Unlike Z_H , however, the difference in ρ_{hv} between S and C bands did not increase with height for outer debris as inner debris were redistributed outward. A slight positive trend in median $Z_{\rm DR}$ with height (Fig. 14e) suggests that the increasing influence of precipitation may offset outward debris transport, resulting in relatively constant $ho_{
m hv}$ with height. Regardless, it can be concluded that outer debris is likely to be smaller than inner debris on the whole at low levels, with the debris characteristics becoming more similar between inner and outer debris at higher elevations because of the fallout and transport of inner debris away from the tornado.

4. Discussion

a. TDS rotation

The lofting, advection, and fallout of debris may result in the rotation of the debris field with height in some, but not all cases. While the rotation of the TDS with height was consistently observed in the Norman–Little Axe tornado, it is uncertain whether this TDS behavior is commonplace among other tornadoes. For example, the Moore–Choctaw tornado, which was observed by OU-PRIME on the same day as the Norman–Little Axe tornado, was nearly circular in the low levels [cf. Fig. 2 in Griffin et al. (2017)] and remained relatively symmetric throughout the lowest 1.5 km ARL, only becoming slightly elongated to the northeast at higher elevation scans up to 2.5 km ARL, which was approximately the top of the observed TDS (not shown).

A small survey of recent tornadoes in the Oklahoma City metropolitan area⁷ observed by KTLX also did not provide many observations of TDS rotation with height. In our brief survey of central Oklahoma cases, there has been at least one instance of TDS rotation with height captured by KTLX. The 19 May 2013 Shawnee, Oklahoma, tornado passed very close to KTLX, and at 2336 UTC, when the tornado was approximately 12 km in range, a north-south-oriented, elongated TDS was observed at 5° elevation (~1 km ARL, Figs. 15a and 15d). The TDS rotated counterclockwise with height such that it was northwest-southeast oriented at 8° (~1.75 km ARL, Figs. 15c and 15f). The counterclockwise rotation of an elongated TDS was similar to the Norman-Little Axe tornado and demonstrates that the behavior of the Norman-Little Axe tornado was not a singular occurrence. In other cases, TDS rotation and elongation may not occur if the storm-relative wind profiles do not veer as strongly or near-tornado vertical motions favor debris fallout rather than lofting.

b. Temporal evolution of polarimetric profiles

Vertical profiles of polarimetric variables presented in the results section were temporally averaged and represented the bulk characteristics of the TDS over a period of just under 10 min. However, some profiles changed drastically over the observation period. For example, within the Norman–Little Axe tornado, 90th percentile OU-PRIME Z_H for inner debris (Fig. 16a) decreased with height at a rate of 7.5 dB km⁻¹ at 2242 UTC (blue line). However, by 2249 UTC (red line), 90th-percentile Z_H only decreased in by ~2 dB over 2.5 km (~1 dB km⁻¹). Additionally, 90th-percentile

⁷The survey included the 19 May 2013 Shawnee tornado (Snyder and Bluestein 2014; Kurdzo et al. 2017; Wienhoff et al. 2018), 20 May 2013 Moore tornado (e.g., Atkins et al. 2014; Kurdzo et al. 2015), and 31 May 2013 El Reno tornado (e.g., Snyder and Bluestein 2014; Wakimoto et al. 2015, 2016; Tanamachi and Heinselman 2016; Bluestein et al. 2018, 2019), which all produced large, deep TDSs near KTLX.

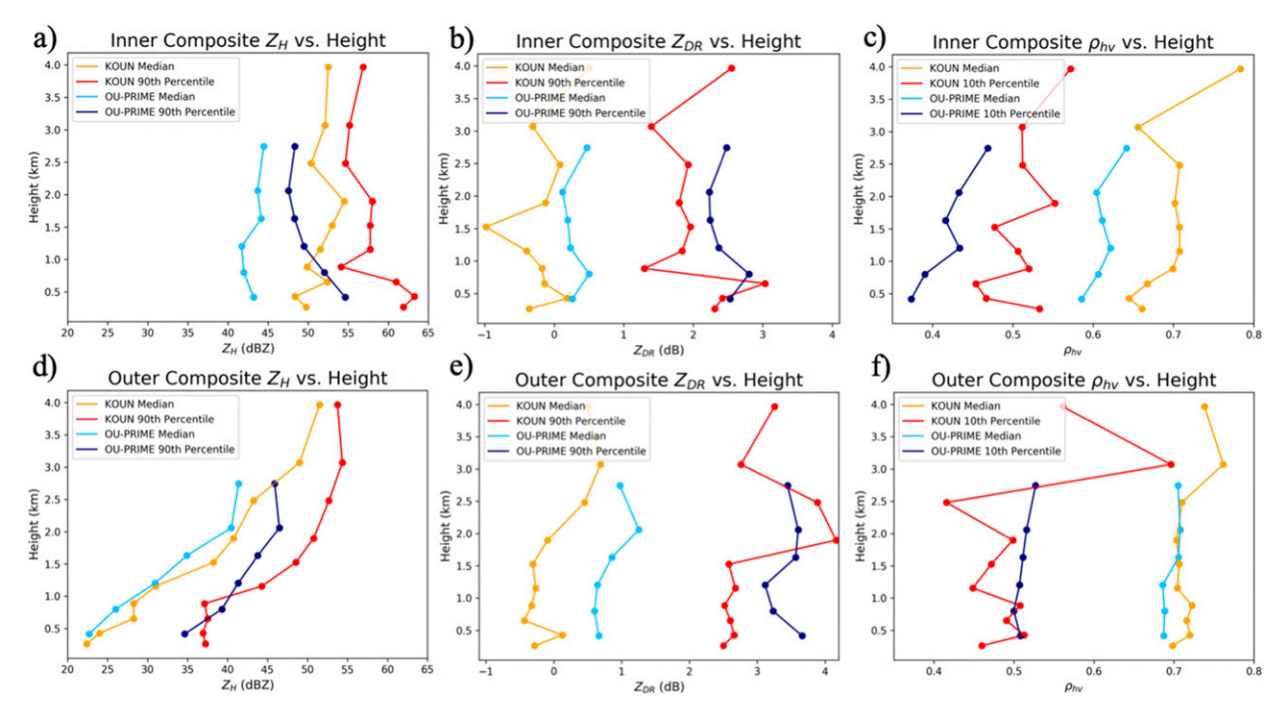


FIG. 14. Composite profiles of (a),(d) reflectivity (dBZ), (b),(e) differential reflectivity (dB), and (c),(f) correlation coefficient vs height (km) for the western tornado valid from 2242 to 2249 UTC, where the profiles are for (top) inner debris (debris within a 1-km radius of the tornado center) and (bottom) debris that is farther than 1 km from the tornado center. Red lines indicate profiles from KOUN (S band), and blue lines are from OU-PRIME (C band). Light colors represent median values, and dark colors represent 90th-percentile values in (a), (b), (d), and (e), and 10th-percentile values in (c) and (f).

 Z_H was at least 5 dB greater at 2249 UTC relative to 2242 UTC for all observed heights. Similarly, median $\rho_{\rm hy}$ (Fig. 16b) increased with height at 2242 UTC (blue line), but the slope of $\rho_{\rm hv}$ decreased with time, and at 2249 UTC (red line) there was no consistent vertical trend. Additionally, median ρ_{hv} decreased at all altitudes with time, which, along with the observed increase in 90th-percentile Z_H , is likely due to the tornado producing greater damage at 2247 and 2249 UTC than at 2242 UTC, consistent with what was observed in Bodine et al. (2013) for other TDS cases. Descriptions of the damage survey from the event (https://www.ncdc.noaa.gov/ stormevents/eventdetails.jsp?id=231948) indicate that the Norman-Little Axe tornado produced increasing damage intensity throughout its life cycle, with the most damage occurring approximately at the end of observation period when the tornado approached the Pottawatomie County, Oklahoma, line. Moreover, observed OU-PRIME ΔV at 1° elevation increased from $\sim 69 \,\mathrm{m\,s}^{-1}$ at 2242 UTC to a maximum of \sim 83 m s⁻¹ at 2247 UTC (Fig. 9) while the beam height increased from 280 to 415 m ARL, respectively.

In general, the profiles in polarimetric variables became more homogeneous with height over time. This may mean that the properties of debris in this column became more homogeneous as well. This could have

been caused by one or a combination of multiple factors. First, the types of debris within the tornado itself could have become less variable over time. At 2242 and 2244 UTC, the Norman-Little Axe tornado was located near the coastline of a large lake, where presumably, fewer large scatterers were available to be lofted. The homogenizing of the profiles during this 8-min period could have been the result of prolonged tornado residency over land at 2247 and 2249 UTC, where damage to trees and anthropogenic structures in Little Axe and the surrounding area introduced a greater quantity of large scatterers (consistent with an increase in Z_H and decrease in $\rho_{\rm hy}$).

Another possible homogenizing factor is that large debris particles, which take longer to ascend, may not have had time to reach the upper portions of the TDS at 2242 UTC, but by 2249 UTC they may have ascended to higher altitudes. Similarly, as the tornado increased in intensity (Fig. 9a), it is likely that it was more capable of lofting larger debris to higher altitudes. The fallout of previously lofted debris from aloft may have acted to homogenize the TDS by counteracting vertical size sorting that occurs when debris are initially lofted (i.e., smaller debris get lofted faster to higher altitudes). Regardless of the responsible mechanism, it does appear that in this particular case

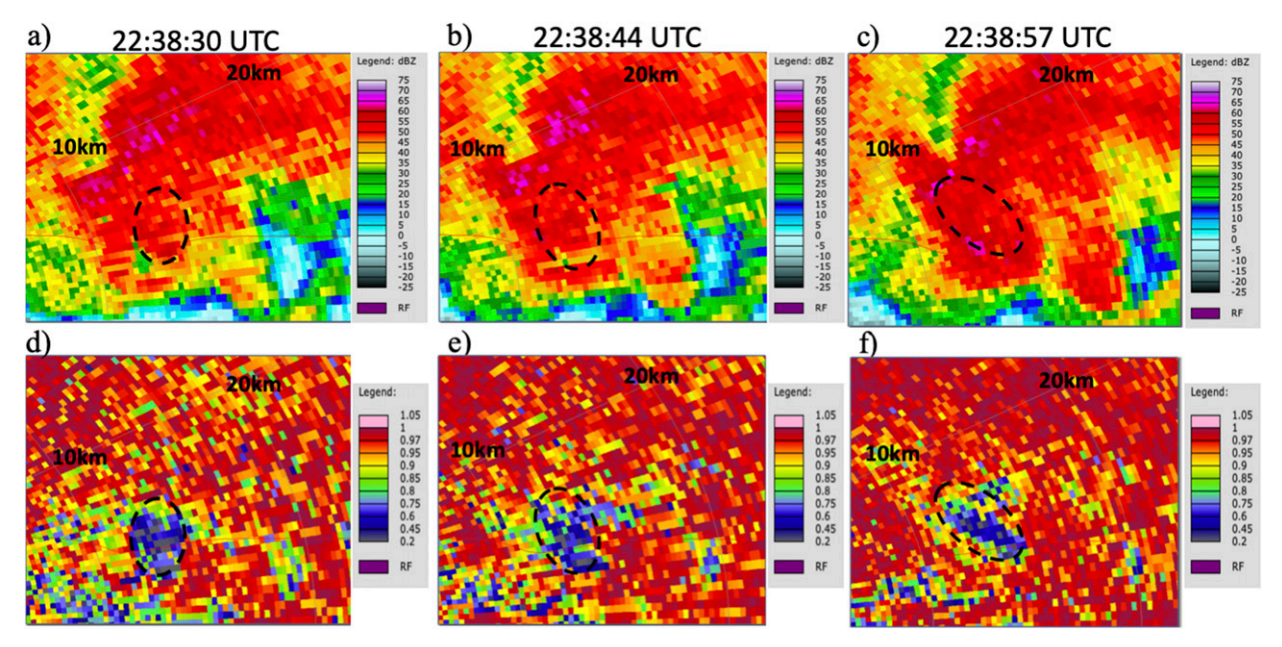


FIG. 15. PPI plots of KTLX (top) reflectivity (dBZ) and (bottom) correlation coefficient at (a),(d) 5°, (b),(e) 6.5°, and (c),(f) 8° elevation valid at 2338 UTC 19 May 2013 for the Shawnee tornado [the plots were generated with the NOAA Weather and Climate Toolkit, available online (https://www.ncdc.noaa.gov/wct/)]. The 10- and 20-km markings and light-gray rings indicate constant range from the radar. The dashed ovals indicate the TDS.

the TDS became much more vertically homogeneous as it became longer lived.

5. Summary and conclusions

The 10 May 2010 tornado outbreak provided a unique opportunity to compare two debris-lofting tornadoes of different intensities that were encountering similar land cover during the analyzed period due to their very close proximity to one another. The Norman–Little Axe tornado produced EF-4 damage and was associated with

the parent mesocyclone of a long-lived supercell. A second tornado located along the gust front of the same supercell produced EF-2 damage. The two tornadoes exhibited contrasting TDS characteristics. The land-spout tornado had high Z_H at its center surrounded by relatively lower Z_H and at one point exhibited an annulus of low $\rho_{\rm hv}$ at the periphery of its TDS. It was determined from a comparison of bulk polarimetric characteristics that median and 90th-percentile Z_H was larger in the Norman–Little Axe tornado, consistent with its greater damage intensity. Median and 90th-percentile $\rho_{\rm hv}$ and

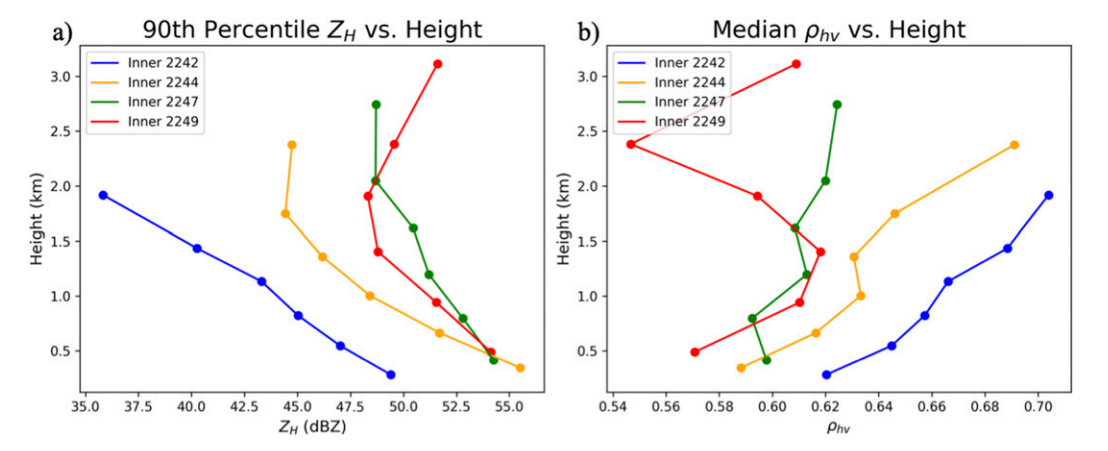


FIG. 16. OU-PRIME (a) 90th-percentile reflectivity (dBZ) and (b) median correlation coefficient vs height (km) valid at 2242 UTC (blue line), 2244 UTC (orange line), 2247 UTC (green line), and 2249 UTC (red line) for debris within 1 km of the Norman–Little Axe tornado.

 Z_{DR} were also higher in the Norman–Little Axe tornado, likely because of precipitation entrainment. Despite differences in the overall magnitude and horizontal distribution of polarimetric variables, in both tornadoes Z_H decreased with height, ρ_{hv} increased with height, and Z_{DR} was relatively constant with height.

The shape of the TDS and spatial distribution of debris within the Norman-Little Axe tornado did change substantially with height. At low levels, the TDS was elongated with an east-west orientation and the majority of the debris located to the east of the tornado. As elevation increased, much of the debris to the east of the tornado was redistributed to the north and to a lesser extent, west, of the tornado. This was a by-product of the TDS rotating and elongating with height such that the major axis of the TDS pointed toward the northeast at higher elevation angles. The rotation of the TDS with height was most prominent at the end of the observation period, when the tornado was producing the most intense damage. It is likely that a strongly veering stormrelative wind profile near the tornado was responsible for the redistribution of debris and TDS rotation with height by detraining and transporting debris in a preferential direction. Additionally, northeastward stormrelative winds above 2 km ARL were likely responsible for the elongation of the TDS in that direction.

A novel dual-wavelength comparison of debris characteristics within the tornado (inner) to debris between 1 and 3 km from the tornado (outer) was performed. This provides a comparison of debris residing within the tornado with debris ejected into the nearby storm-scale flow (e.g., storm-scale updraft, RFD). The S-band Z_H was found to be larger than C-band Z_H for both inner and outer debris, with the greatest dual-wavelength differences occurring for debris within the tornado. This is likely due to larger debris being present within the tornado and is consistent with previous observations (Bodine et al. 2014) and simulations of debris radar signatures (Bodine et al. 2016) that showed such differences result from resonance effects of large particles. In general, Z_H was lower and ρ_{hv} was higher for outer debris, which, coupled with smaller dual-wavelength differences, suggests that outer debris was smaller than inner debris. The dual-wavelength difference in Z_H increased with height for outer debris, and inner and outer Z_H values at both wavelengths became much more similar at upper levels. This is likely due to debris within the tornado being redistributed outward with height from the effects of centrifuging and advection away from the center of the tornado by the mean wind.

As can be seen in this and other recent studies, it may be possible to infer some characteristics of the neartornado wind field based solely on observations of debris

using polarimetric radars (e.g., veering storm-relative wind profiles inferred from the elongation and rotation of the TDS). While many of the findings in this study are intuitive, more cases are needed to know whether observations like the differences in the debris characteristics of inner and outer debris can be generalized. Moreover, it appears that only a subset of TDSs rotate with height, and additional dual-Doppler and highresolution model datasets are needed to investigate the kinematic controls on this particular debris behavior. Observations and polarimetric radar simulations with much finer scale spatial and temporal resolution are needed to investigate and better understand the relationships between tornado intensity and structure and the manifestation of TDS appendages, polarimetric inhomogeneities, and the vertical distribution of debris.

Acknowledgments. This study was supported by the National Science Foundation under Grant AGS-1823478. The authors thank Boonleng Cheong, Sebastian Torres, Caleb Fulton, and the three anonymous reviewers for input on improving this work. We also thank the Advanced Radar Research Center engineers for maintaining OU-PRIME and thank Boonleng Cheong for operating the radar on 10 May 2010.

REFERENCES

Atkins, N. T., K. M. Butler, K. R. Flynn, and R. M. Wakimoto, 2014: An integrated damage, visual, and radar analysis of the 2013 Moore, Oklahoma, EF-5 tornado. *Bull. Amer. Meteor. Soc.*, **95**, 1549–1561, https://doi.org/10.1175/BAMS-D-14-00033.1.

Balakrishnan, N., and D. S. Zrnić, 1990: Use of polarization to characterize precipitation and discriminate large hail. *J. Atmos. Sci.*, **47**, 1525–1540, https://doi.org/10.1175/1520-0469(1990) 047<1525:UOPTCP>2.0.CO;2.

Barnes, S., 1964: A technique for maximizing details in numerical weather map analysis. *J. Appl. Meteor.*, **3**, 396–409, https://doi.org/10.1175/1520-0450(1964)003<0396:ATFMDI>2.0.CO;2.

Barnes, S. L., 1973: Mesoscale objective map analysis using weighted time-series. NOAA Tech. Memo. ERL NSSL-62, 60 pp., https://repository.library.noaa.gov/view/noaa/17647.

Batt, R. G., M. P. Petach, S. A. Peabody II, and R. R. Batt, 1999: Boundary layer entrainment of sand-sized particles at high speed. J. Fluid Mech., 392, 335–360, https://doi.org/10.1017/ S0022112099005510.

Bluestein, H. B., M. M. French, R. L. Tanamachi, S. Frasier, K. Hardwick, F. Junyent, and A. Pazmany, 2007: Close-range observations of tornadoes in supercells made with a dualpolarization, X-band, mobile Doppler radar. *Mon. Wea. Rev.*, 135, 1522–1543, https://doi.org/10.1175/MWR3349.1.

—, K. J. Thiem, J. C. Snyder, and J. B. Houser, 2018: The multiple-vortex structure of the El Reno, Oklahoma, tornado on 31 May 2013. *Mon. Wea. Rev.*, **146**, 2483–2502, https:// doi.org/10.1175/MWR-D-18-0073.1.

---, ---, and ---, 2019: Tornadogenesis and early tornado evolution in the El Reno, Oklahoma, supercell on 31 May

- 2013. Mon. Wea. Rev., **147**, 2045–2066, https://doi.org/10.1175/MWR-D-18-0338.1.
- Bodine, D. J., M. R. Kumjian, R. D. Palmer, P. L. Heinselman, and A. V. Ryzhkov, 2013: Tornado damage estimation using polarimetric radar. *Wea. Forecasting*, 28, 139–158, https://doi.org/ 10.1175/WAF-D-11-00158.1.
- —, R. D. Palmer, and G. Zhang, 2014: Dual-wavelength polarimetric radar analyses of tornadic debris signatures. J. Appl. Meteor. Climatol., 53, 242–261, https://doi.org/ 10.1175/JAMC-D-13-0189.1.
- ——, T. Maruyama, C. Fulton, Y. Zhu, and B. L. Cheong, 2016: Simulated frequency dependence of radar observations of tornadoes. *J. Atmos. Oceanic Technol.*, 33, 1825–1842, https:// doi.org/10.1175/JTECH-D-15-0120.1.
- Bringi, V. N., V. Chandrasekar, N. Balakrishnan, and D. S. Zrnić, 1990: An examination of propogation effects in rainfall on radar measurements at microwave frequencies. *J. Atmos. Oceanic Technol.*, 7, 829–840, https://doi.org/10.1175/1520-0426(1990) 007<0829:AEOPEI>2.0.CO;2.
- Dowell, D. C., C. R. Alexander, J. M. Wurman, and L. J. Wicker, 2005: Centrifuging of hydrometeors and debris in tornadoes: Radar-reflectivity patterns and wind-measurement errors. *Mon. Wea. Rev.*, 133, 1501–1524, https://doi.org/10.1175/MWR2934.1.
- French, M. M., D. Burgess, E. R. Mansell, and L. Wicker, 2015: Bulk hook echo raindrop sizes retrieved using mobile, polarimatric Doppler radar observations. *J. Appl. Meteor. Clima*tol., 54, 423–450, https://doi.org/10.1175/JAMC-D-14-0171.1.
- Griffin, C. B., D. J. Bodine, and R. D. Palmer, 2017: Kinematic and polarimetric radar observations of the 10 May 2010, Moore-Choctaw, Oklahoma, tornadic debris signature. *Mon. Wea. Rev.*, 145, 2723–2741, https://doi.org/10.1175/ MWR-D-16-0344.1.
- Houser, J. L., H. B. Bluestein, and J. Snyder, 2016: A finescale radar examination of the tornadic debris signature and weak-echo reflectivity band associated with a large, violent tornado. *Mon. Wea. Rev.*, 144, 4101–4130, https://doi.org/ 10.1175/MWR-D-15-0408.1.
- Knox, J. A., and Coauthors, 2013: Tornado debris characteristics and trajectories during the 27 April 2011 super outbreak as determined using social media data. *Bull. Amer. Meteor. Soc.*, 94, 1371–1380, https://doi.org/10.1175/BAMS-D-12-00036.1.
- Koch, S. E., M. desJardins, and P. J. Kocin, 1983: An interactive Barnes objective map analysis scheme for use with satellite and conventional data. J. Climate Appl. Meteor., 22, 1487–1503, https://doi.org/10.1175/1520-0450(1983)022<1487: AIBOMA>2.0.CO;2.
- Kumjian, M. R., 2011: Precipitation properties of supercell hook echoes. *Electron. J. Severe Storms Meteor.*, 6 (5), https://ejssm.org/ojs/index.php/ejssm/article/viewArticle/93.
- —, and A. V. Ryzhkov, 2008: Polarimetric signatures in supercell thunderstorms. J. Appl. Meteor. Climatol., 47, 1940–1961, https://doi.org/10.1175/2007JAMC1874.1.
- Kurdzo, J. M., D. J. Bodine, B. L. Cheong, and R. D. Palmer, 2015: High-temporal resolution polarimetric X-band Doppler radar observations of the 20 May 2013 Moore, Oklahoma, tornado. *Mon. Wea. Rev.*, 143, 2711–2735, https://doi.org/10.1175/ MWR-D-14-00357.1.
- —, and Coauthors, 2017: Observations of severe local storms and tornadoes with the Atmospheric Imaging Radar. *Bull. Amer. Meteor. Soc.*, 98, 915–935, https://doi.org/10.1175/BAMS-D-15-00266.1.
- Magsig, M. A., and J. T. Snow, 1998: Long-distance debris transport by tornadic thunderstorms. Part I: The 7 May 1995 supercell

- thunderstorm. *Mon. Wea. Rev.*, **126**, 1430–1449, https://doi.org/ 10.1175/1520-0493(1998)126<1430;LDDTBT>2.0.CO;2.
- Majcen, M., P. Markowski, Y. Richardson, D. Dowell, and J. Wurman, 2008: Mulipass objective analyses of Doppler radar data. J. Atmos. Oceanic Technol., 25, 1845–1858, https:// doi.org/10.1175/2008JTECHA1089.1.
- Nolan, D. S., 2013: On the use of Doppler radar-derived wind fields to diagnose the secondary circulations of tornadoes. *J. Atmos. Sci.*, **70**, 1160–1171, https://doi.org/10.1175/JAS-D-12-0200.1.
- Oye, R., C. Mueller, and S. Smith, 1995: Software for radar translation, visualization, editing, and interpolation. Preprints, *27th Conf. on Radar Meteorology*, Vail, CO, Amer. Meteor. Soc., 359–361.
- Palmer, R. D., and Coauthors, 2011: The 10 May 2010 tornado outbreak in central Oklahoma: Potential for new science with high-resolution polarimetric radar. *Bull. Amer. Meteor. Soc.*, 92, 871–891, https://doi.org/10.1175/2011BAMS3125.1.
- Pauley, P. M., and X. Wu, 1990: The theoretical, discrete, and actual response of the Barnes objective scheme for one- and twodimensional fields. *Mon. Wea. Rev.*, 118, 1145–1163, https:// doi.org/10.1175/1520-0493(1990)118<1145:TTDAAR>2.0.CO;2.
- Picca, J., and A. Ryzhkov, 2012: A dual-wavelength polarimetric analysis of the 16 May 2010 Oklahoma City extreme hailstorm. *Mon. Wea. Rev.*, 140, 1385–1403, https://doi.org/10.1175/ MWR-D-11-00112.1.
- Ryzhkov, A. V., D. Burgess, D. Zrnić, T. Smith, and S. Giangrande, 2002: Polarimetric analysis of a 3 May 1999 tornado. Preprints, 21st Conf. on Severe Local Storms, San Antonio, TX, Amer. Meteor. Soc., 14.2, https://ams.confex.com/ams/SLS_WAF_NWP/ techprogram/paper_47348.htm.
- —, T. J. Schuur, D. W. Burgess, and D. S. Zrnić, 2005: Polarimetric tornado detection. J. Appl. Meteor., 44, 557–570, https://doi.org/10.1175/JAM2235.1.
- Schultz, C. J., and Coauthors, 2012a: Dual-polarization tornadic debris signatures Part I: Examples and utility in an operational setting. *Electron. J. Operational Meteor.*, 13, 120–137.
- —, and Coauthors, 2012b: Dual-polarization tornadic debris signatures Part II: Comparisons and caveats. *Electron.* J. Operational Meteor., 13, 138–158.
- Snow, J. T., A. L. Wyatt, A. K. McCarthy, and E. K. Bishop, 1995: Fallout of debris from tornadic thunderstorms: A historical perspective and two examples from VORTEX. *Bull. Amer. Meteor. Soc.*, 76, 1777–1790, https://doi.org/10.1175/ 1520-0477(1995)076<1777:FODFTT>2.0.CO;2.
- Snyder, J. C., and H. Bluestein, 2014: Some considerations for the use of high-resolution mobile radar data in tornado intensity determination. Wea. Forecasting, 29, 799–827, https://doi.org/ 10.1175/WAF-D-14-00026.1.
- ——, and A. V. Ryzhkov, 2015: Automated detection of polarimetric tornado debris signatures using a hydrometeor classification algorithm. *J. Appl. Meteor. Climatol.*, **54**, 1861–1870, https://doi.org/10.1175/JAMC-D-15-0138.1.
- Tanamachi, R. L., and P. L. Heinselman, 2016: Rapid-scan, polarimetric observations of central Oklahoma severe storms on 31 May 2013. Wea. Forecasting, 31, 19–42, https://doi.org/10.1175/WAF-D-15-0111.1.
- Umeyama, A., B. L. Cheong, S. Torres, and D. Bodine, 2018: Orientation analysis of simulated tornadic debris. J. Atmos. Oceanic Technol., 35, 993–1010, https://doi.org/10.1175/ JTECH-D-17-0140.1.
- Van Den Broeke, M. S., 2015: Polarimetric tornadic debris signature variability and debris fallout signatures. J. Appl. Meteor. Climatol., 54, 2389–2405, https://doi.org/10.1175/JAMC-D-15-0077.1.

- ——, and S. T. Jauernic, 2014: Spatial and temporal characteristics of polarimetric tornadic debris signatures. *J. Appl. Meteor. Climatol.*, **53**, 2217–2231, https://doi.org/10.1175/JAMC-D-14-0094.1.
- Wakimoto, R. M., N. T. Atkins, and J. Wurman, 2011: The LaGrange tornado during VORTEX2. Part I: Photogrammetric analysis of the tornado combined with single-Doppler data. *Mon. Wea. Rev.*, 139, 2233–2258, https://doi.org/10.1175/ 2010MWR3568.1.
- ——, P. Stauffer, W. C. Lee, N. T. Atkins, and J. Wurman, 2012: Finescale structure of the LaGrange, Wyoming, tornado during VORTEX2: GBVTD and photogrammetric analyses. *Mon. Wea. Rev.*, 140, 3397–3418, https://doi.org/10.1175/MWR-D-12-00036.1.
- —, N. T. Atkins, K. M. Butler, H. B. Bluestein, K. Thiem, J. Snyder, and J. Houser, 2015: Photogrammetric analysis of the 2013 El Reno tornado combined with mobile X-band polarimetric radar data. *Mon. Wea. Rev.*, 143, 2657–2683, https://doi.org/10.1175/MWR-D-15-0034.1.
- —, and Coauthors, 2016: Areal damage survey of the 2013 El Reno tornado combined with mobile radar data. *Mon. Wea. Rev.*, **144**, 1749–1776, https://doi.org/10.1175/MWR-D-15-0367.1.

- —, Z. Wienhoff, H. B. Bluestein, and D. Reif, 2018: The Dodge City tornadoes on 24 May 2016: Damage survey, photogrammetric analysis combined with mobile polarimetric radar data. *Mon. Wea. Rev.*, 146, 3735–3771, https://doi.org/10.1175/ MWR-D-18-0125.1.
- WDTB, 2013: Dual-polarization radar training. NOAA/National Weather Service Warning Decision Training Branch, accessed 10 May 2019, https://training.weather.gov/wdtd/courses/dualpol/Outreach/.
- Wienhoff, Z. B., H. B. Bluestein, L. J. Wicker, J. C. Snyder, A. Shapiro, C. K. Potvin, J. B. Houser, and D. W. Reif, 2018: Applications of a spatially variable advection correction technique for temporal correction of dual-Doppler analyses of tornadic supercells. *Mon. Wea. Rev.*, 146, 2949–2971, https:// doi.org/10.1175/MWR-D-17-0360.1.
- Wurman, J., J. Straka, and E. Rasmussen, 1996: Fine-scale Doppler radar observations of tornadoes. *Science*, 272, 1774–1777, https://doi.org/10.1126/science.272.5269.1774.
- Zrnić, D. S., and A. V. Ryzhkov, 1999: Polarimetry for weather surveillance radars. *Bull. Amer. Meteor. Soc.*, **80**, 389–406, https://doi.org/10.1175/1520-0477(1999)080<0389:PFWSR>2.0.CO;2.